

Stellar Feedback in Galaxies and the Origin of Galaxy-scale Winds

Philip F. Hopkins^{*1}, Eliot Quataert¹, & Norman Murray^{2,3}

¹Department of Astronomy and Theoretical Astrophysics Center, University of California Berkeley, Berkeley, CA 94720

²Canadian Institute for Theoretical Astrophysics, 60 St. George Street, University of Toronto, ON M5S 3H8, Canada

³Canada Research Chair in Astrophysics

Submitted to MNRAS, September, 2011

ABSTRACT

Feedback from massive stars is believed to play a critical role in driving galactic super-winds that enrich the intergalactic medium and shape the galaxy mass function, mass-metallicity relation, and other global galaxy properties. In previous papers, we have introduced new numerical methods for implementing stellar feedback on sub-GMC through galactic scales in numerical simulations of galaxies; the key physical processes include radiation pressure in the UV through IR, supernovae (Type-I & II), stellar winds (“fast” O star through “slow” AGB winds), and HII photoionization. Here, we show that these feedback mechanisms drive galactic winds with outflow rates as high as $\sim 10 - 20$ times the galaxy star formation rate. The mass-loading efficiency (wind mass loss rate divided by the star formation rate) scales roughly as $\dot{M}_{\text{wind}}/\dot{M}_* \propto V_c^{-1}$ (where V_c is the galaxy circular velocity), consistent with simple momentum-conservation expectations. We use our suite of simulations to study the relative contribution of each feedback mechanism to the generation of galactic winds in a range of galaxy models, from SMC-like dwarfs and Milky-way analogues to $z \sim 2$ clumpy disks. In massive, gas-rich systems (local starbursts and high- z galaxies), radiation pressure dominates the wind generation. By contrast, for MW-like spirals and dwarf galaxies the gas densities are much lower and sources of shock-heated gas such as supernovae and stellar winds dominate the production of large-scale outflows. In all of our models, however, the winds have a complex multi-phase structure that depends on the interaction between multiple feedback mechanisms operating on different spatial and time scales: any *single* feedback mechanism fails to reproduce the winds observed. We use our simulations to provide fitting functions to the wind mass-loading and velocities as a function of galaxy properties, for use in cosmological simulations and semi-analytic models. These differ from typically-adopted formulae with an explicit dependence on the gas surface density that can be very important in both low-density dwarf galaxies and high-density gas-rich galaxies.

Key words: galaxies: formation — star formation: general — galaxies: evolution — galaxies: active — cosmology: theory

1 INTRODUCTION

Feedback from massive stars is critical to the evolution of galaxies. In cosmological models of galaxy evolution without strong stellar feedback, gas rapidly cools and turns into stars, leading to galaxies with star formation rates much higher than observed, and \sim ten times the stellar mass found in real galaxies (e.g. Katz et al. 1996; Somerville & Primack 1999; Cole et al. 2000; Springel & Hernquist 2003b; Kereš et al. 2009a, and references therein). Simply suppressing the rate of star formation does not solve the problem: the amount of baryons in real galactic disks is much lower than the amount of cool gas in disks found in cosmological simulations, especially in low-mass galaxies (White & Frenk 1991; for a recent review see Kereš et al. 2009b). Constraints from the mass-metallicity relation and enrichment of the IGM also imply that the baryons

cannot simply be prevented from entering galaxy halos along with dark matter (Tremonti et al. 2004; Erb et al. 2006; Aguirre et al. 2001; Pettini et al. 2003; Songaila 2005). Some process must very efficiently remove baryons from galaxies.

Related problems appear on smaller spatial and time scales. The Kennicutt-Schmidt (KS) law implies that star formation is very slow within galaxies, with a gas consumption time of ~ 50 dynamical times (Kennicutt 1998). Moreover, the integrated fraction of mass turned into stars in GMCs over their lifetime is only a few to several percent (Zuckerman & Evans 1974; Williams & McKee 1997; Evans 1999; Evans et al. 2009). Without strong stellar feedback, however, self-gravitating collapse leads to most of the gas turning into stars in just a few dynamical times.

The problem, then, on both galactic and sub-galactic scales, is twofold. First, star formation must be “slowed down” at a given global/local gas surface density. But this alone would still violate integral constraints, producing galaxies and star clusters more mas-

* E-mail:phopkins@astro.berkeley.edu

sive than observed by an order of magnitude. Thus the second problem: on small scales gas must be expelled from GMCs, and on galactic scales either prevented from entering, or, more likely in our judgment, removed from, the host galaxy. In other words, local outflows and global super-winds must be generated that can remove gas at a rate rapid compared to the star formation rate.

Because low-mass galaxies are preferentially baryon-poor, matching the faint end of the observed galaxy mass function in cosmological simulations requires that the global efficiency of galactic super-winds scales as a declining power of galaxy mass or circular velocity. Oppenheimer & Davé (2006) and Oppenheimer et al. (2010) find that an average scaling $\dot{M}_{\text{wind}}/\dot{M}_* \propto V_c^{-1}$ produces reasonably good agreement with the observed mass functions at different redshifts,¹ with a normalization such that an SMC-mass dwarf has a mass loading $\dot{M}_{\text{wind}}/\dot{M}_* \sim 10$ (although this scaling may still over-produce the number of very low-mass galaxies). Large mass-loading factors of several times the SFR are also estimated in even relatively massive local galaxies and massive star-forming regions at $z \sim 2 - 3$ (Martin 1999, 2006; Heckman et al. 2000; Newman et al. 2012; Sato et al. 2009; Chen et al. 2010; Steidel et al. 2010; Coil et al. 2011).

The scaling $\dot{M}_{\text{wind}}/\dot{M}_* \propto V_c^{-1}$ is expected from momentum conservation arguments, given a number of simplifying assumptions and sufficient global momentum input from supernovae, stellar winds, radiation pressure, etc. (Murray et al. 2005). Direct observations, while uncertain, tend to favor velocity and \dot{M}_{wind} scalings similar to this constraint for the bulk of the outflowing gas (Martin 2005; Rupke et al. 2005; Weiner et al. 2009).

To date, however, numerical simulations have generally not been able to produce, from an *a priori* model, winds with either such large absolute mass loading factors or the scaling of mass-loading with galaxy mass/velocity. Many simulations, lacking the ability to directly resolve the relevant feedback processes, put in winds “by hand” by e.g. forcing an outflow rate that scales in a user-specified manner with the star formation rate or other parameters (Springel & Hernquist 2003a; Oppenheimer & Davé 2008; Sales et al. 2010; Genel et al. 2012). Alternatively, models that self-consistently include stellar feedback have generally been limited to a small subset of the relevant processes; the vast majority include only thermal feedback via supernovae (i.e. thermal energy injection with some average rate that scales with the mass in young stars). However, thermal feedback is very inefficient in the dense regions where star formation occurs, and in the ISM more broadly in gas-rich galaxies. For this reason, such models require further changes to the physics in order for thermal energy injection to have a significant effect. Often cooling (along with star formation and other hydrodynamic processes) is “turned off” for an extended period of time (Thacker & Couchman 2000; Governato et al. 2007; Brook et al. 2011). With or without these adjustments, however, such models generally obtain winds that are weaker than those required to explain the galaxy mass function, especially at low masses (see e.g. Guo et al. 2010; Powell et al. 2011; Brook et al. 2011; Nagamine 2010, and references therein).

In our view, part of the resolution of this difficulty lies in the treatment of the ISM physics *within* galaxies. Feedback processes other than supernovae are critical for suppressing star formation in

¹ Note that the agreement we speak of is with the faint sub- L_* end of the mass function. It is widely agreed that different physics, perhaps AGN feedback, is critical for the regulation of the bright super- L_* end of the mass function. We focus here on stellar feedback and star-forming systems.

dense gas; these include protostellar jets, HII regions, stellar winds, and radiation pressure from young stars. Including these mechanisms self-consistently maintains a reasonable fraction of the ISM at densities where the thermal heating from supernovae has a larger effect. This conclusion implies that (not surprisingly) a realistic treatment of galactic winds requires a more realistic treatment of the stellar feedback processes that maintain the multi-phase structure of the ISM of galaxies.

Motivated by this perspective, in Hopkins et al. (2011) (Paper I) and Hopkins et al. (2012) (Paper II) we developed a new set of numerical models to follow feedback on small scales in GMCs and star-forming regions, in simulations with pc-scale resolution.² These simulations include the momentum imparted locally (on sub-GMC scales) from stellar radiation pressure, radiation pressure on larger scales via the light that escapes star-forming regions, HII photoionization heating, as well as the heating, momentum deposition, and mass loss by SNe (Type-I and Type-II) and stellar winds (O star and AGB). The feedback is tied to the young stars, with the energetics and time-dependence taken directly from stellar evolution models. Our models also include realistic cooling to temperatures < 100 K, and a treatment of the molecular/atomic transition in gas and its effect on star formation (following Krumholz & Gnedin 2011).

We showed in Papers I & II that these feedback mechanisms produce a quasi-steady ISM in which giant molecular clouds form and disperse rapidly, after turning just a few percent of their mass into stars. This leads to an ISM with phase structure, turbulent velocity dispersions, scale heights, and GMC properties (mass functions, sizes, scaling laws) in reasonable agreement with observations. In this paper, we use these same models of stellar feedback to quantitatively predict the elusive winds invoked in almost all galaxy formation models.

The remainder of this paper is organized as follows. In § 2 we summarize the galaxy models we use and our methods of implementing stellar feedback. In § 3 we discuss how each feedback mechanism affects the morphology, phase structure, and velocity distribution of galactic winds. In § 4, we discuss the mass-loading of winds and how the mass loss rate depends on the inclusion of different feedback mechanisms. We further determine how the outflow rate scales with galaxy properties and use our simulations to derive more accurate approximations to wind scalings for use in cosmological simulations and semi-analytic models. In § 5 we summarize our results and discuss their implications.

2 METHODS

The simulations used here are described in detail in Paper I (see their Section 2 and Tables 1-3) and Paper II (their Section 2). However we briefly summarize the most important properties of the models here. The simulations were performed with the parallel TreeSPH code GADGET-3 (Springel 2005). They include stars, dark matter, and gas, with cooling, star formation, and stellar feedback.

Gas follows a standard atomic cooling curve but in addition can cool to < 100 K via fine-structure cooling. This allows it to collapse to very high densities, and star formation occurs in dense regions above a threshold $n > 1000 \text{ cm}^{-3}$, with a rate $\dot{\rho}_* = \epsilon \rho / t_{\text{ff}}$ where t_{ff} is the free-fall time and $\epsilon = 1.5\%$ is an efficiency taken from observations of star-forming regions with the same densities

² Movies of these simulations are available at <https://www.cfa.harvard.edu/~phopkins/Site/Research.html>

(Krumholz & Tan 2007, and references therein). We further follow Krumholz & Gnedin (2011) and calculate the molecular fraction within the dense gas as a function of the local column density and metallicity, and allow star formation only from that gas. In Paper I we show that the SFR is essentially independent of the small-scale star formation law (robust to large variations in the threshold and efficiency, and changes in the power-law index $\dot{\rho} \propto \rho^{1-2}$). This is because star formation is feedback-regulated and dense star-forming regions grow in mass until sufficient new stars have formed to halt further collapse. Likewise in Paper II we show that the corrections from the molecular chemistry are negligible at the masses and metallicities we model.

2.1 Disk Models

Our calculations span four distinct initial disk models, designed to represent a range of characteristic galaxy types. Each initial disk has a bulge, stellar and gaseous disk, and dark matter halo. The disks are initialized in equilibrium so that in the absence of cooling, star formation, and feedback there are no significant transients. The gaseous disk is initially vertically pressure-supported, but this thermal energy is radiated away in much less than a dynamical time and the emergent vertical structure depends on feedback. Our “low” resolution runs (used to evolve the simulations for several Gyr, to ensure steady-state behavior) use $\approx 3 \times 10^6$ particles, with $\approx 10^6$ particles in the disk, giving SPH smoothing lengths of ~ 10 pc in the central few kpc of a MW-like disk (the smoothing length scales linearly with the disk size/mass scale). Our “standard” resolution cases use ~ 30 times as many particles, and correspondingly have $\sim 1 - 5$ pc smoothing lengths and particle masses of $500 M_\odot$; these are run for a few orbital times each. A few ultra-high resolution runs used for convergence tests employ $\sim 10^9$ particles, with sub-pc resolution on kpc scales.

(1) SMC: an SMC-like dwarf, with baryonic mass $M_{\text{bar}} = 8.9 \times 10^8 M_\odot$ and halo mass $M_{\text{halo}} = 2 \times 10^{10} M_\odot$ (concentration $c = 15$), a Hernquist (1990) profile bulge with a mass $m_b = 10^7 M_\odot$, and exponential stellar ($m_d = 1.3 \times 10^8 M_\odot$) and gas disks ($m_g = 7.5 \times 10^8 M_\odot$) with scale-lengths $h_d = 0.7$ and $h_g = 2.1$ kpc, respectively. The initial stellar scale-height is $z_0 = 140$ pc and the stellar disk is initialized such that the Toomre $Q = 1$ everywhere. The gas and stars are initialized with uniform metallicity $Z = 0.1 Z_\odot$.

(2) MW: a MW-like galaxy, with halo and baryonic properties of $(M_{\text{halo}}, c) = (1.6 \times 10^{12} M_\odot, 12)$ and $(M_{\text{bar}}, m_b, m_d, m_g) = (7.1, 1.5, 4.7, 0.9) \times 10^{10} M_\odot$, $Z = Z_\odot$, and scale-lengths $(h_d, h_g, z_0) = (3.0, 6.0, 0.3)$ kpc.

(3) Sbc: a LIRG-like galaxy (i.e. a more gas-rich spiral than is characteristic of those observed at low redshifts) with $(M_{\text{halo}}, c) = (1.5 \times 10^{11} M_\odot, 11)$, $(M_{\text{bar}}, m_b, m_d, m_g) = (10.5, 1.0, 4.0, 5.5) \times 10^9 M_\odot$, $Z = 0.3 Z_\odot$, and $(h_d, h_g, z_0) = (1.3, 2.6, 0.13)$ kpc.

(4) HiZ: a high-redshift massive starburst disk, chosen to match the properties of the observed non-merging but rapidly star-forming SMG population, with $(M_{\text{halo}}, c) = (1.4 \times 10^{12} M_\odot, 3.5)$ and a virial radius appropriately rescaled for a halo at $z = 2$ rather than $z = 0$, $(M_{\text{bar}}, m_b, m_d, m_g) = (10.7, 0.7, 3, 7) \times 10^{10} M_\odot$, $Z = 0.5 Z_\odot$, and $(h_d, h_g, z_0) = (1.6, 3.2, 0.32)$ kpc.

2.2 Feedback Models

The most important physics in these simulations is the model of stellar feedback. We include feedback from a variety of mechanisms, each of which we briefly describe below. More details about our implementations of this physics are given in Paper I and Paper II. We use a Kroupa (2002) initial mass function (IMF) throughout and use STARBURST99 (Leitherer et al. 1999) to calculate the

stellar luminosity, mass return from stellar winds, supernova rate, etc. as a function of the age and metallicity of each star particle.

(1) **Local Momentum Deposition** from Radiation Pressure, Supernovae, & Stellar Winds: In Paper I, we present the radiation pressure aspect of this model for feedback from young star clusters in detail. At each timestep, gas particles identify the nearest density peak representing the center of the nearest star-forming “clump” or GMC-analog. We calculate the total luminosity of the star particles inside the sphere defined by the distance from the center of this star-forming region to the gas particle of interest; the incident flux on the gas is then determined assuming that the local star forming region is optically thick to the UV radiation.

The rate of momentum deposition from radiation pressure is then $\dot{P}_{\text{rad}} \approx (1 + \tau_{\text{IR}}) L_{\text{incident}}/c$ where the term $1 + \tau_{\text{IR}}$ accounts for the fact that most of the initial optical/UV radiation is absorbed and re-radiated in the IR; $\tau_{\text{IR}} = \Sigma_{\text{gas}} \kappa_{\text{IR}}$ is the optical depth in the IR, which allows for the fact that the momentum is boosted by multiple scatterings in optically thick regions. Here Σ_{gas} is calculated self-consistently as the average surface density of the identified clump, with $\kappa_{\text{IR}} \approx 5 (Z/Z_\odot) g^{-1} \text{cm}^2$ approximately constant over the relevant physical range of dust temperatures. The imparted acceleration is directed along the flux vector. In Paper I we discuss numerous technical aspects of this implementation – such as the effects of resolution, photon leakage, and how the momentum is discretized – and show that essentially all our conclusions are robust to uncertainties in these choices.

The *direct* momentum of SNe ejecta and stellar winds \dot{P}_{SNe} and \dot{P}_w are similarly tabulated from STARBURST99 and injected as an appropriate function of age and metallicity to the gas within a smoothing length of each star. This source of turbulent energy is almost always smaller than that due to radiation pressure discussed above. In some cases, however, in particular in dwarf galaxies, the work done by bubbles of gas shock-heated by supernovae and/or stellar winds is dynamically important; this is discussed below.

(2) **Supernova and Stellar Wind Shock-Heating:** The gas shocked by supernovae and stellar winds can be heated to high temperatures, generating bubbles and filaments of hot gas. We tabulate the Type-I and Type-II SNe rates from Mannucci et al. (2006) and STARBURST99, respectively, as a function of age and metallicity for all star particles, and stochastically determine at each timestep if a SNe occurs. That is, the SNe are resolved discretely in time (as opposed to continuous energy injection). For each SNe, the appropriate thermal energy is injected into the gas within a smoothing length of the star particle. Similarly, stellar winds are assumed to shock locally and so we inject the appropriate tabulated mechanical power $L(t, Z)$ as a continuous function of age and metallicity into the gas within a smoothing length of the star particles. The specific energy of these stellar winds is large for young stellar populations in which fast winds from massive stars dominate, but declines rapidly at later times when slower, AGB winds dominate.

(3) **Gas Recycling:** Gas mass is returned continuously to the ISM from stellar evolution, at a rate tabulated from SNe and stellar mass loss in STARBURST99. The integrated mass fraction recycled is ~ 0.3 .

(4) **Photo-Heating of HII Regions:** For each star particle, we tabulate the rate of production of ionizing photons from STARBURST99. Starting from the nearest gas particle and working our way outwards radially from the star, we then ionize each gas particle which is not already ionized until the photon budget is exhausted (using the gas and stellar properties to determine the photon production rate needed to maintain the particle as fully ionized). Gas which is ionized is immediately heated to $\sim 10^4$ K, unless is

already above this temperature; moreover, the gas is not allowed to cool below 10^4 K until it is no longer in an HII region. This method allows for overlapping, non-spherical HII regions that can extend to radii \sim kpc.

(5) **Long-Range Radiation Pressure:** Radiation pressure from photons absorbed in the immediate vicinity of stars is captured in mechanism (1). However, photons that escape these regions can still be absorbed at larger radii. For each star particle, we construct the intrinsic SED (L_ν) as a function of age and metallicity; we then use the local density and density gradients to estimate the integrated column density and attenuation of the SED using $\tau_\nu = \kappa_\nu \Sigma \approx \kappa_\nu \rho (h_{\text{sml}} + |\nabla \ln \rho|^{-1})$, where h_{sml} is the smoothing length and κ_ν is the frequency-dependent opacity (assuming dust opacities that scale with metallicity, as in (1) above). The resulting “escaped” SED gives a frequency-dependent flux \mathbf{F}_ν that is propagated to large distances. We construct a force tree for this long range force in an identical fashion to the gravity tree, since after attenuating the flux near the star particle, the stellar flux is assumed to decrease $\propto r^{-2}$. Each gas particle then sees an incident net flux vector \mathbf{F}'_ν , integrated over all stars in the galaxy.

Extensive numerical tests of the feedback models are presented in Paper I and Paper II. In the Appendix, we present additional numerical and convergence studies specific to galactic winds.

3 WIND MORPHOLOGIES & PHASE STRUCTURE

3.1 Morphologies with Feedback

Figure 1 shows the stellar and gas morphology for each galaxy model in our standard simulations with all feedback mechanisms included. All cases exhibit clear outflows. The stellar maps show a mock *ugr* composite image in which the spectrum of each star particle is calculated from its age and metallicity, and the dust extinction/reddening is accounted for from the line-of-sight dust mass (following Hopkins et al. 2005). The gas maps show the projected gas density (intensity) and temperature (color, with blue representing cold molecular gas at $T \lesssim 1000$ K, pink representing the warm ionized gas at $\sim 10^4 - 10^5$ K, and yellow representing the hot, X-ray emitting gas at $\gtrsim 10^6$ K).

The HiZ models result in disks with massive ($> 10^8 M_\odot$) \sim kpc-scale clumps, similar to “clump-chain” systems. Violent outflows arise from throughout the disk driven by the very high rate of star formation, with $\dot{M}_* > 100 M_\odot \text{ yr}^{-1}$. The outflow is clearly multi-phase: there is a volume-filling hot component (largely from hot gas “venting” out of SNe-heated regions and from “fast” OB stellar winds), but most of the mass is in dense clumps, filaments, and streams. We quantify this more in §3.5.

The Sbc models also produce clumpy gas structure but on smaller scales and with the global structure more closely tracing spiral arms. This is similar to observed dwarf starbursts (e.g. NGC 1569 or 1313). Again, a multi-phase super-wind is evident, arising from the reasonably high specific star formation rate of $\dot{M}_*/M_* \sim 0.2 - 1 \text{ Gyr}^{-1}$.

In the MW models, which are much more gas poor than the HiZ and Sbc models, the gas in the edge-on image traces the stellar spiral and bar instabilities, albeit with filamentary and clumpy GMC structure internal to the arms. The outflows here are less clearly multi-phase; with the low specific SFR and gas fraction, much of the material is directly “vented” hot gas, rather than accelerated cold material.

The SMC models have a patchy ISM typical of dwarf irregular

systems, with large overlapping SNe bubbles. Outflows above the thick disk appear as a mix of venting hot gas and shells of warm material accelerated by the hot gas; the latter appear visually as loops, shells, and filaments of gas.

3.2 Effects of Each Feedback Mechanism in Turn

Figure 2 shows the edge-on wind morphologies of models that include different feedback mechanisms, but are otherwise identical.

First consider the HiZ model. If we view the disk face-on (see Paper II), the clumpy morphology seen in Figure 1 is evident in all cases (this arises from violent gravitational instability); however, without momentum from radiation pressure, the characteristic sizes of individual clumps collapse from \sim kpc to \sim pc and the gas piles up at densities $\sim 10^6 \text{ cm}^{-3}$. Supernovae, stellar wind momentum, and HII photoionization pressure are not sufficiently strong to resist the collapse of clumps beyond a critical threshold and the cooling time in these dense regions is much too short for thermal pressure to be important. Some hot gas is produced from star clusters that have nearly exhausted their gas supply. This vents directly out of the disk producing the hot gas seen in the right-most image in Figure 2, but the warm/cold material in the wind – most of the wind mass – is almost totally absent.

If we instead turn off sources of gas heating (SNe, stellar wind shock-heating, and HII photo-heating), the primary difference relative to our standard run is in the volume-filling diffuse phase (the properties interior to dense clumps are nearly identical). The diffuse gas is much cooler (note the absence of yellow gas in the middle panel), but the warm clumps in the outflow – most of the wind mass – remain, directly accelerated out of the disk by radiation pressure.

For the MW-analogue model without radiation pressure, GMCs again collapse to significantly smaller sizes, although the runaway is not as severe because “fast” stellar winds and HII heating are able to somewhat suppress runaway GMC collapse (see Paper II). Some wind material in the cold phase is also absent, but this is not the dominant wind phase in the full simulations, so the net difference is much weaker than in the HiZ case. Removing the sources of heating has a comparable effect on the SFR as removing the radiation pressure (Paper II), but it removes the volume-filling “hot” gas and dramatically suppresses the wind (middle panel in Fig. 2); there is thus little material accelerated by radiation pressure alone in MW-like models.

Figure 2 shows that the Sbc case lies, as expected, somewhere between the MW and HiZ cases in terms of the contribution of the different feedback processes to the galaxy-scale outflow. In the SMC-like model, on the other hand, the average gas density is very low ($\lesssim 0.1 \text{ cm}^{-3}$), approaching the regime in which the cooling time can be comparable to the dynamical time. In addition, with the lower densities and metallicities the IR optical depths are not large. As a result, with only radiation pressure present, there is no hot gas and essentially no wind. Turning off SNe heating, by contrast, has a large effect – the volume filling factor of hot gas “bubbles” drops, and the wind is basically absent.

3.3 Appearance in X-Rays

X-ray observations of canonical systems such as M82 provide a strong probe of the shock-heated phase of galactic winds. We therefore consider some of the X-ray properties of our simulated galactic outflows. For convenience, rather than making a detailed mock observation corresponding to a given instrument, sensitivity, redshift,

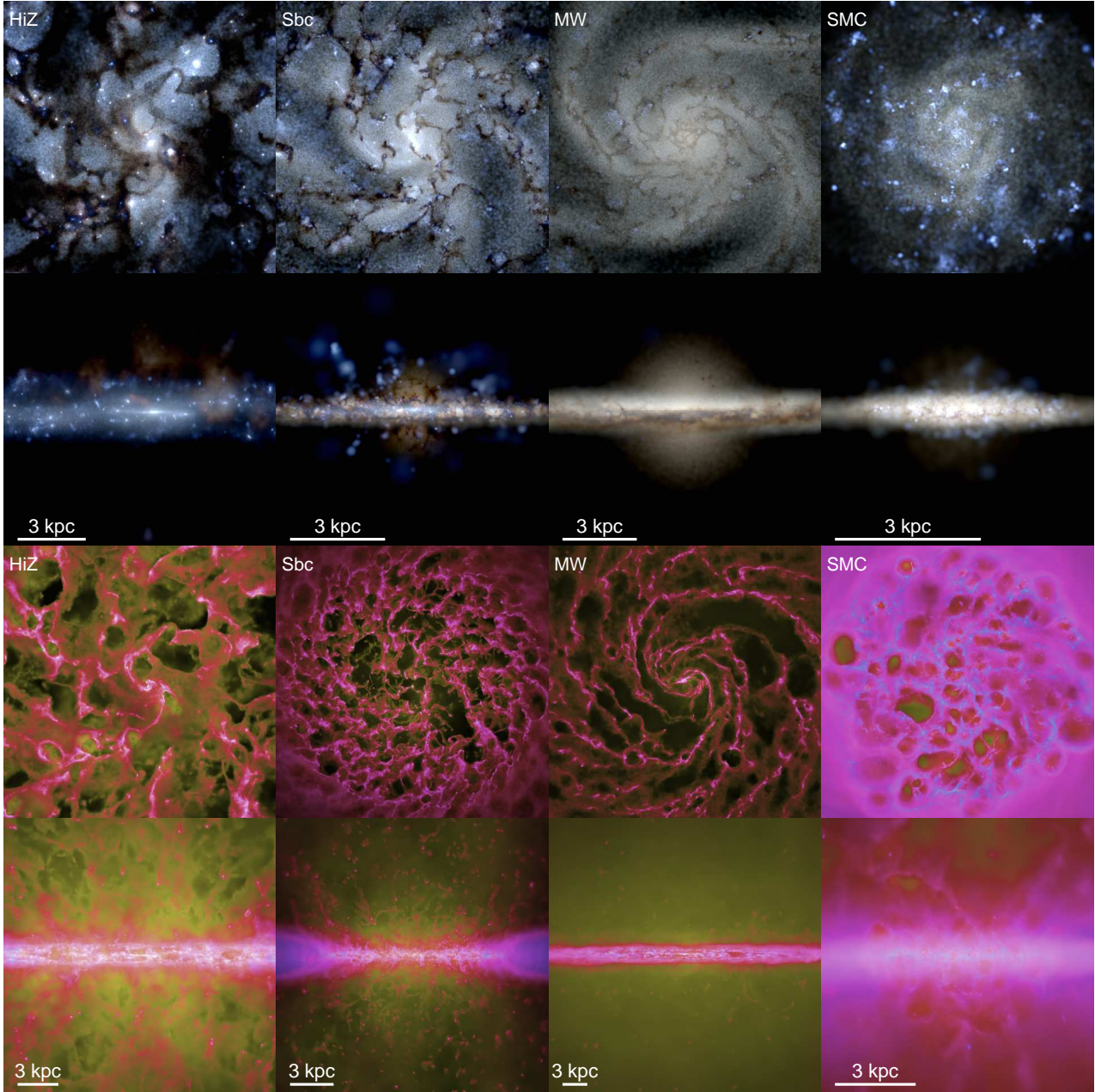


Figure 1. Morphology of the gas & stars in our standard simulations with all feedback mechanisms enabled; we show face-on and edge-on projections. The time in each is ~ 2 orbital times after the simulation begins, when the disk is in a feedback-regulated steady state. **Top:** Stars. We show a mock ugr (SDSS-band) composite, with stellar spectra calculated from their known ages and metallicities and including dust attenuation. Brightness is logarithmically scaled with a ≈ 2 dex stretch. **Bottom:** Gas. Brightness encodes projected gas density (logarithmically scaled with a ≈ 4 dex stretch); color encodes gas temperature with blue being $T \lesssim 1000$ K molecular gas, pink $\sim 10^4 - 10^5$ K warm ionized gas, and yellow $\gtrsim 10^6$ K hot gas. Each column corresponds to one of our four galaxy models. **HiZ:** A massive, $z \sim 2 - 4$ starburst disk with $\dot{M}_* > 100 M_\odot \text{ yr}^{-1}$; gravitational collapse forms kpc-scale complexes and a clumpy morphology, with violent outflows containing dense, cold gas driven by the massive starburst. **Sbc:** A $z \sim 0$ dwarf starburst galaxy; the disk is clumpy but more contained in global spiral structure, with outflows from the central few kpc producing a multi-phase clumpy wind. **MW:** A MW-analogue; the gas morphology more closely follows stars in a global spiral pattern; the “wind” here is primarily hot SNe-driven bubbles/holes “venting” out, rather than the clumpy filaments/streamers seen in the HiZ/Sbc cases. **SMC:** An isolated SMC-analogue dwarf; the disk is thick with irregular star formation and large bubbles from overlapping SNe; the wind is prominent and contains a mix of hot gas and entrained cold/warm material in filaments/loops/arcs. The “smooth” outer disk is ionized and low-density, sufficient to prevent collapse at these masses.

and energy range, we instead quantify the thermal bremsstrahlung emission, for which the emissivity per unit volume is

$$u_X \propto T_{\text{gas}}^{1/2} n_e n_i \quad (1)$$

where T_{gas} is the gas temperature and n_e and n_i are the number density of electrons and ions. At fixed pressure, u_X is typically dominated by the lowest temperature gas and so equation 1 need not refer specifically to X-ray observations. We quantify the contributions of gas at different temperatures to the thermal emission

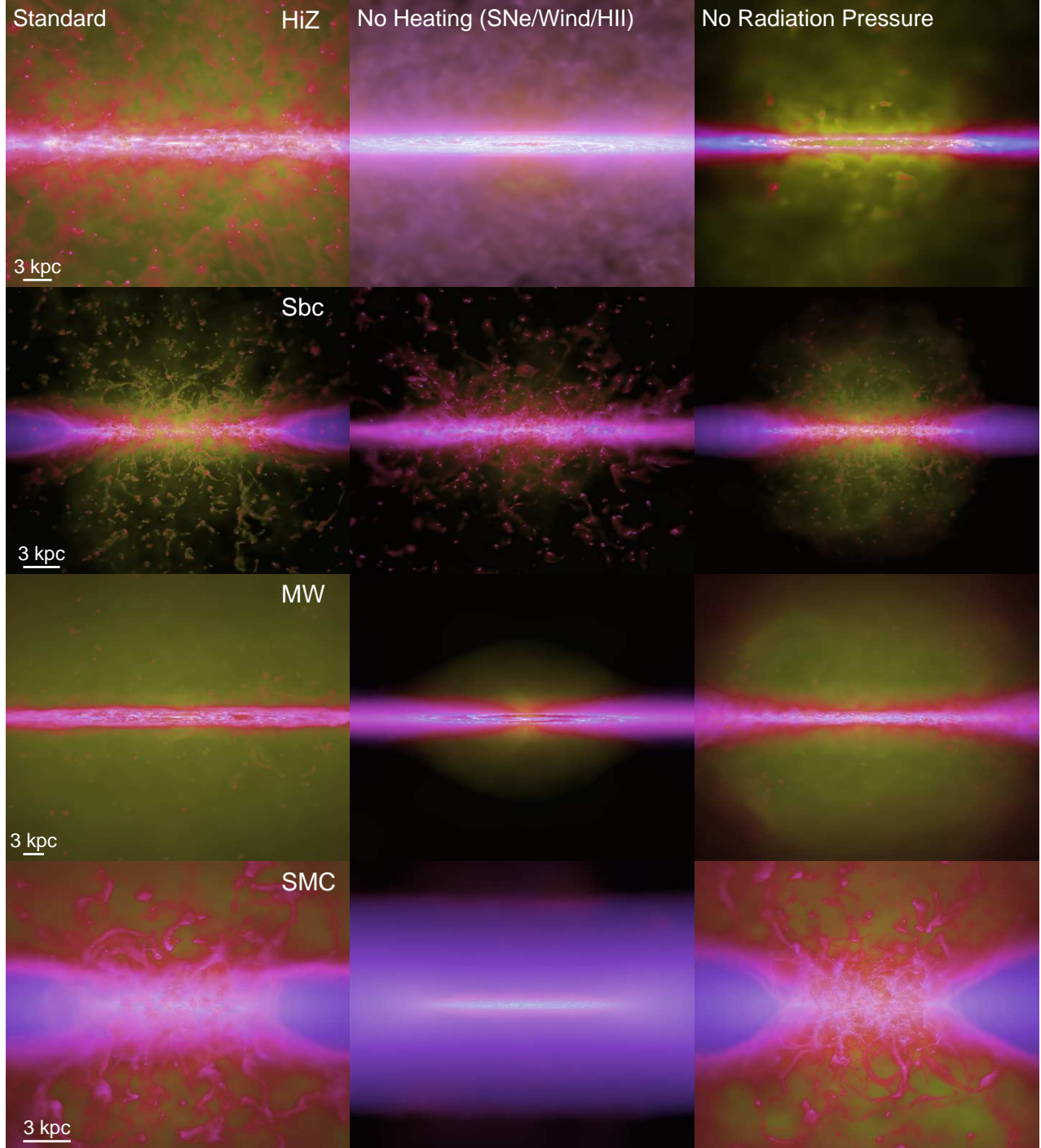


Figure 2. Edge-on gas morphologies (as Fig. 1), with different feedback mechanisms enabled. *Left:* Standard model (all feedback on). *Middle:* No heating: energy injection from SNe, shocked stellar winds, and HII photo-heating is disabled (gas recycling from these mechanisms remains, but is “cold”). The “hot” volume-filling ISM is greatly diminished but in the HiZ/Sbc cases the global morphology and much of the wind mass (in the cold/clumpy phase) remains. In the MW/SMC cases, removing heating eliminates most of the wind mass (including warm gas, previously accelerated by hot gas). *Right:* No radiation pressure momentum flux (local or long-range). The hot medium remains, but in the HiZ/Sbc cases most of the cold/warm clumpy material in the wind is absent (hot gas simply vents). The wind in the MW/SMC cases is less strongly affected, but within the disk, GMCs collapse much further than they would with radiation pressure, giving a higher SFR at the same absolute wind mass.

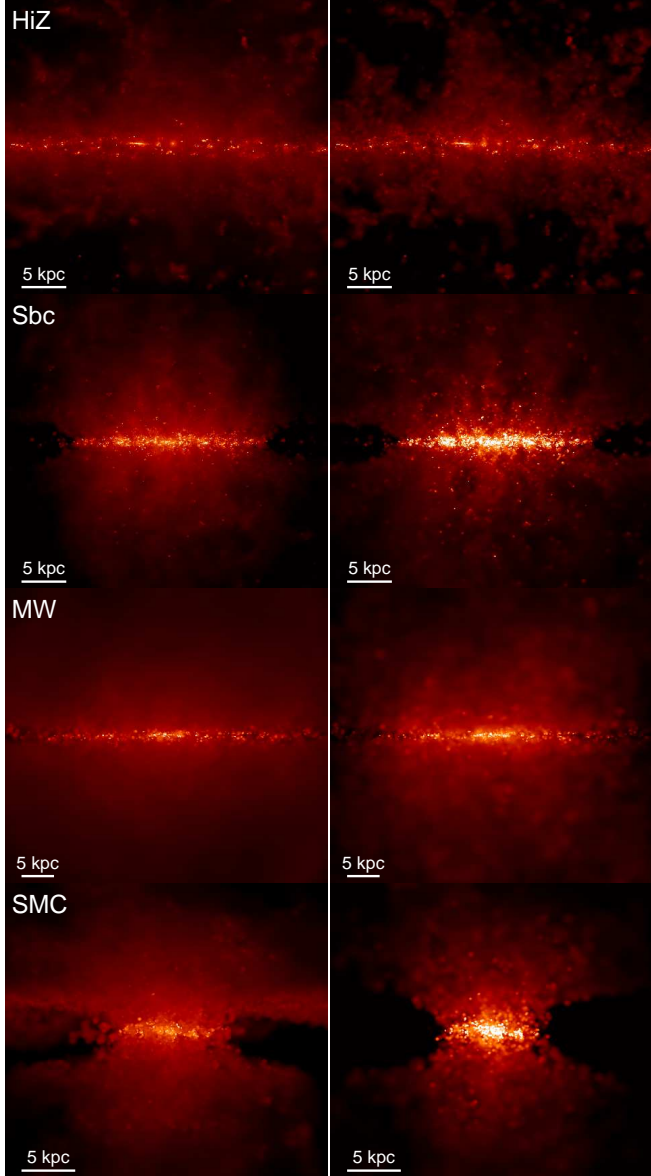


Figure 3. *Left:* Galactic wind thermal emission morphology, as a proxy for X-ray emission. The maps show edge-on images of our standard models for each disk (with all feedback enabled). Intensity here encodes the projected bremsstrahlung emissivity (eq. 1). A roughly bi-conical, clumpy/multiphase wind is typical, similar to that observed in, e.g., M82. *Right:* Same, but now showing the metal cooling luminosity. Note the enhanced clumpiness from the inhomogenous metal distribution.

below. To start, however, Figure 3 shows the observed morphology of the winds for our fiducial simulation of each galaxy model, with surface brightness weighted (logarithmically) using the thermal emission in equation 1 (using the known temperature, density, and ionization information in the simulations). Very broadly, the appearance of the winds in Figure 3 is similar to that seen in Figure 1, but the clumpy structure of the winds is more evident and the global morphology is more obviously bi-conical (since much of the in-plane material is neutral and so does not appear here). Overall, the morphologies of the Sbc and SMC-like models are qualitatively similar to observations of systems like M82. The HiZ case is more spatially extended, making the outflow less columnar. The

MW model is less clearly wind-like but is instead consistent with a diffuse halo.

The top panel of Figure 4 shows $dL_X/d\ln T_{\text{gas}}$, the contribution of gas at different temperatures to the total thermal bremsstrahlung emission. This weighting favors dense cool gas given roughly comparable pressures at different temperatures, but there is a rapid cut-off below $\sim 10^4$ K because the gas becomes neutral. Figure 4 shows that much of the "x-ray" emission would be contributed by gas at $\sim 10^6 - 10^7$ K with the exact range of temperatures depending on the system. Figure 4 also divides $dL_X/d\ln T_{\text{gas}}$ into intervals in radial outflow velocity. The material at low $v_r < 10 \text{ km s}^{-1}$ (including negative v_r) is generally non-outflowing gas at the cooler end of the temperature distribution. At higher radial velocities, the thermal emission tends to come preferentially from higher-temperature gas. We show below that in the very high-velocity wind, much of the mass is in the form of warm gas, but the thermal emission shown here is primarily sensitive to the hotter material.

We caution that the dominant cooling emission for gas with $T_{\text{gas}} \sim 10^6 - 10^7$ K probably comes from metal lines, not thermal bremsstrahlung. Our treatment of enrichment in the current models is relatively simple and just traces the total metallicity (improved models will be presented in future work in preparation); therefore it is difficult to make detailed predictions for the line emission. However, we can use the compiled tables presented in Wiersma et al. (2009), who use a suite of CLOUDY calculations to determine the total metal-cooling luminosity as a function of n_e , n_i , Z (assuming solar abundance ratios), T_{gas} and the photo-ionizing UV background (for simplicity the $z = 0$ background is used), to calculate the metal cooling luminosity. We plot the morphology of this emission as well in Figure 3. It is broadly similar to the thermal bremsstrahlung emission, as expected; however, the metal-line emission is significantly more clumpy (and in the Sbc case more concentrated in vertical filamentary structures as well) – closer to what is actually observed in systems like M82. This is because the metals are inhomogeneous. We caution, however, that metal diffusion and other small-scale mixing processes are not followed here, so the degree of inhomogeneity may be over-estimated.

3.4 Velocity and Column Density Distributions

Figure 4 (middle panel) also plots the radial velocity distribution of gas in the simulations, specifically the mass per unit radial velocity dm/dv_r . There is a concentration of gas at small $|v_r|$ which is the rotationally-supported disk (this includes almost all the star-forming gas). This "spike" is symmetric about $v_r = 0$; the winds appear as the large excess of material at $v_r \gg 0$, extending to $v_r > 1000 \text{ km s}^{-1}$ even in the SMC-like case.

In each galaxy model, the winds span a wide range in outflow velocity – there is no single “wind velocity” (contrary to what is assumed in many models). The distribution of mass in dm/dv_r has a broad plateau up to some “turnover” velocity, above which it falls off more rapidly; we can approximate it with

$$\frac{dm_{\text{wind}}}{dv_r} \propto \frac{1}{1 + (v_r/v_0)^\alpha} \quad (2)$$

with $\alpha \sim 3 - 7$ and $v_0 \sim 800, 500, 200$, and 200 km s^{-1} in the HiZ, Sbc, MW, and SMC cases, respectively. For comparison, the maximum circular velocities of these systems are $V_{\text{max}} \approx 230, 86, 190$ and 46 km s^{-1} . In the starburst systems where radiation pressure is critical for much of the wind (HiZ/Sbc), the turnover velocity is a few times V_{max} (comparable to the escape velocity) – this is expected for radiatively accelerated winds. In contrast, the maximum

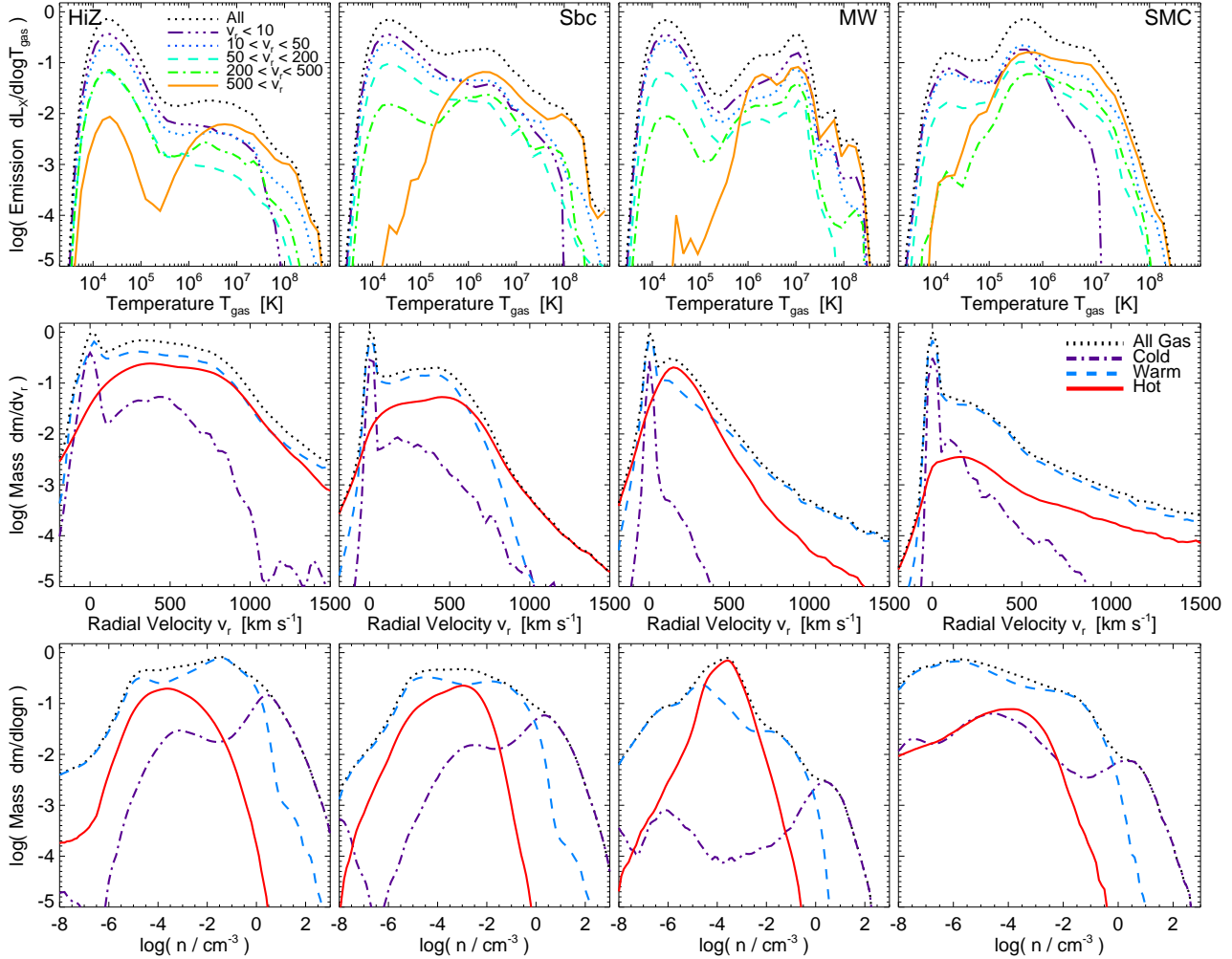


Figure 4. Top: Thermal bremsstrahlung emission-weighted distribution of gas temperature $dL_X/d\log T_{\text{gas}}$. For each galaxy model (columns), we show results for our standard simulation with all feedback mechanisms (time-averaged over the simulation). Different lines in a given panel correspond to gas with different radial velocities (relative to the center of mass). The emission from more rapidly outflowing wind material tends to be dominated by the hotter gas with $T \sim 10^{6-8} \text{ K}$. Middle: Mass-weighted distribution of gas outflow radial velocities dm/dv_r . The distribution for all gas is divided into the contribution from different phases: cold (primarily molecular) ($T < 2000 \text{ K}$), warm (primarily ionized) ($2000 < T < 4 \times 10^5 \text{ K}$) and hot diffuse ($T > 4 \times 10^5 \text{ K}$) gas. The high v_r part of the distribution is the wind material, with a distribution that can be fit by equation 2. This outflowing gas consists primarily of a mix of warm and hot gas with some colder (likely molecular) material. The warm material usually dominates the mass, and is in the form of the dense clouds, filaments, and shells seen in Figure 1. Bottom: Mass-weighted density distribution for the unbound wind material, divided into different phases as in the middle panel. The cold/warm/hot gas dominates at high/intermediate/low densities, respectively. The “warm” material at very low densities, $\ll 10^{-4} \text{ cm}^{-3}$ is previously “hot” material that has adiabatically cooled as it expands; these low densities arise artificially because we do not include an IGM into which the wind expands.

velocities in the lower-SFR systems appear to asymptote to a maximum at a few hundred km s^{-1} – such a roughly constant velocity is, in turn, the expectation for thermally heated galactic outflows.

Observationally, the column density distribution of the gas is probed directly by absorption line measurements (e.g., Na and Mg lines). Figure 5 quantifies this distribution in our simulations. To calculate this, we determined the average column density distribution calculated over ~ 100 different projections of the galaxy, each time calculating the integrated line-of-sight column along $\sim 10^4$ sightlines through an aperture of fixed physical radius about the galaxy center (uniformly sampling the aperture area). Note this calculation is simply the total hydrogen column density – we do not include the ionization corrections that are critical to computing realistic line strengths. The very large columns in Figure 5 come from the few percent of sightlines which go through the disks, but the bulk of the column density distribution is domi-

nated by the winds. Figure 5 shows that there is a broad range of columns with a roughly power-law behavior in N_H at low values (expected for an expanding, constant \dot{M} wind); the characteristic columns range from $\sim 10^{18} - 10^{20} \text{ cm}^{-2}$ around dwarf galaxies to $\sim 10^{20} - 10^{22} \text{ cm}^{-2}$ around massive systems.

3.5 Cold, Warm, and Hot Outflows

The mass distribution as a function of radial velocity in Figure 4 divides the gas into three traditional phases with a simple temperature cut: “cold atomic+molecular” gas ($T < 2000 \text{ K}$), “warm ionized” gas ($2000 < T < 4 \times 10^5 \text{ K}$) and “hot” gas ($T > 4 \times 10^5 \text{ K}$). The wind is a mix of warm gas (containing most of the mass) and volume-filling hot gas, with a few percent contribution from cold gas at all velocities. This is shown directly in the lower panel of Figure 4, where we consider the density distribution of wind mate-

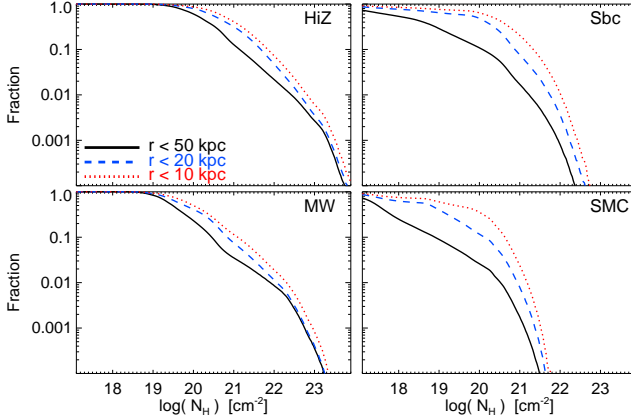


Figure 5. Cumulative distribution of gas column density (fraction $> N_H$) along random sightlines within different radii around each galaxy in our simulations with all feedback mechanisms. The results are averaged over time and projected disk angle, for random sightlines within a projected circular aperture of physical radius r around the disk center (labeled). The few percent of sightlines at large columns ($\gtrsim 10^{22} \text{ cm}^{-2}$) go through the disk itself; the remainder are dominated by wind material. Wind material with $N_H \gtrsim 10^{19} \text{ cm}^{-2}$ has a large covering factor within a few tens of kpc, and there is a broad range of columns $\sim 10^{18} - 10^{21} \text{ cm}^{-2}$.

rial (defined as all unbound gas, see below), divided into these same phases. The wind includes material with a broad range of densities $n \sim 10^{-6} - 10^2 \text{ cm}^{-3}$, with high-density material at $n \gtrsim 1 \text{ cm}^{-3}$ primarily “cold,” intermediate-density material ($n \sim 0.01 - 1 \text{ cm}^{-3}$) “warm,” and low-density material ($n \lesssim 0.01 \text{ cm}^{-3}$) “hot.”

The instantaneous phase structure in the wind is not the same, however, as the phase structure of the material at the time it was initially accelerated into the wind. Its multi-phase origin is evident in the fact that the warm gas is highly inhomogenous; most of the mass is at a density $\sim 20 - 100$ times higher than would be expected if it were smoothly distributed over a spherical shell (the formal clumping factor is $\langle \rho^2 \rangle / \langle \rho \rangle^2 \approx 100$ in each case). Some of the warm gas – especially in the larger and more diffuse loops and shells, is material from the diffuse “warm-phase” of the disk disk (which has both sizeable mass and volume filling factors) directly accelerated out of the disk. But the large tail of very low-density ($n \lesssim 10^{-4} \text{ cm}^{-3}$) volume-filling warm gas is material initially launched as “hot” gas, which cools adiabatically as it expands. And much of the dense clumpy/filamentary structure is material initially launched as “cold” gas, which rapidly becomes photo-ionized as it expands and its average density falls.

There are several important numerical caveats to the micro-scale phase structure in the wind shown here. In particular, acceleration of cold gas directly by hot gas is difficult to treat accurately in SPH codes, and comparison with adaptive mesh schemes suggests that we are likely to under-estimate the true amount of cold material in the wind (Springel 2010; Keres et al. 2011). Similarly, we do not capture the thermal evaporation of cold gas to form hot gas or the condensation of hot gas to form cool gas. And the adiabatic expansion of the gas to extremely low densities is possible because our simulations do not include a realistic IGM into which the gas would expand. As a result, the phase distributions shown in Figure 4 are unlikely to be quantitatively accurate.

4 MASS-LOADING OF GALACTIC WINDS

4.1 Effects of Each Feedback Mechanism in Turn

From the broader perspective of galaxy formation, the most important integral property of galaxy winds is probably the total wind mass outflow rate. This is typically quantified in terms of its ratio to the star formation rate $\dot{M}_{\text{wind}}/\dot{M}_*$, i.e. the wind mass per unit mass of stars formed. Figure 6 shows the wind masses of our models, in a series of otherwise identical simulations with different feedback mechanisms enabled or disabled in turn. This quantifies the importance of a given feedback process in driving the wind in our simulations. We compare the total mass in the wind M_{wind} as a function of time, relative to the integrated mass in stars formed since the start of the simulation M_{new} – the ratio of these quantities $M_{\text{wind}}/M_{\text{new}}$ defines the average “global” wind efficiency $\langle \dot{M}_{\text{wind}} \rangle / \langle \dot{M}_* \rangle$. If we evaluate the instantaneous efficiency or average in narrow time bins, we obtain similar results but with increasing scatter.

In these calculations, we define the “wind” as material with a positive Bernoulli parameter $b \equiv (v^2 + 3 c_s^2 - v_{\text{esc}}^2)/2$, i.e., material that would escape in the absence of additional forces or cooling.³

Figure 6 shows that for the HiZ galaxy model, the photon momentum plays a critical role in driving much of the wind mass. By contrast, removing the sources of hot gas (SNe, stellar winds, and HII heating) has little effect on the total wind mass. With all feedback mechanisms operating, a multi-phase wind is blown with an outflow rate between $\sim 0.2 - 1$ times the SFR. Without local and long-range acceleration by photon momentum, however, the wind efficiency drops by a factor of ~ 5 , both because the absolute wind mass drops and because the star formation rate increases significantly. The long-range acceleration due to the ambient radiation field is especially critical in driving the wind: we show in Paper II that a moderate increase in the UV escape fraction from the galaxy can increase the wind mass by factors of $\sim 2 - 5$. By contrast, removing the local IR radiation pressure support within star forming regions has a much weaker effect on the wind (though we have shown in Paper I that it is critical for the support of GMC complexes themselves). The winds in the HiZ model therefore seem not to be directly launched from GMCs, but rather are the result of a two step process (Murray et al. 2011). First, UV and IR radiation pressure lifts up gas parcels. Second, these parcels are then continuously accelerated by photons emerging from the entire disk, rather than only those from their natal GMC.

For the MW model, our fiducial calculations produce a wind with an outflow rate a couple times the SFR.⁴ The relative role of the hot wind phase is much more prominent than in the HiZ case. If we remove all of the thermal feedback (SNe, stellar winds, and HII

³ We have also calculated the wind mass using a more observationally accessible definition: material that has reached at least $> 500 \text{ pc}$ above the disk, with absolute outflow velocity $> 100 \text{ km s}^{-1}$. This gas may or may not all be formally unbound, and the exact “cuts” in z and v are arbitrary, but we find that this definition of wind mass is generally within $\sim 20\%$ of the wind mass defined with the Bernoulli parameter. Moreover, the results are essentially unchanged for moderate (factor ~ 2) changes in the threshold values of z and v .

⁴ The high wind mass-loading at early times ($\dot{M}_{\text{wind}} \sim 10 \dot{M}_*$) is partially an artifact of the initial conditions. This occurs in part because it takes $\sim 2 \times 10^8 \text{ yr}$ for the SFR to reach equilibrium, and partly because the pre-simulation bulge+disk stars are initialized with a broad age range, so a small fraction are sufficiently young to have a large feedback effect before the SFR rises much (and because the galaxy is so gas-poor, this has as a proportionally large effect).

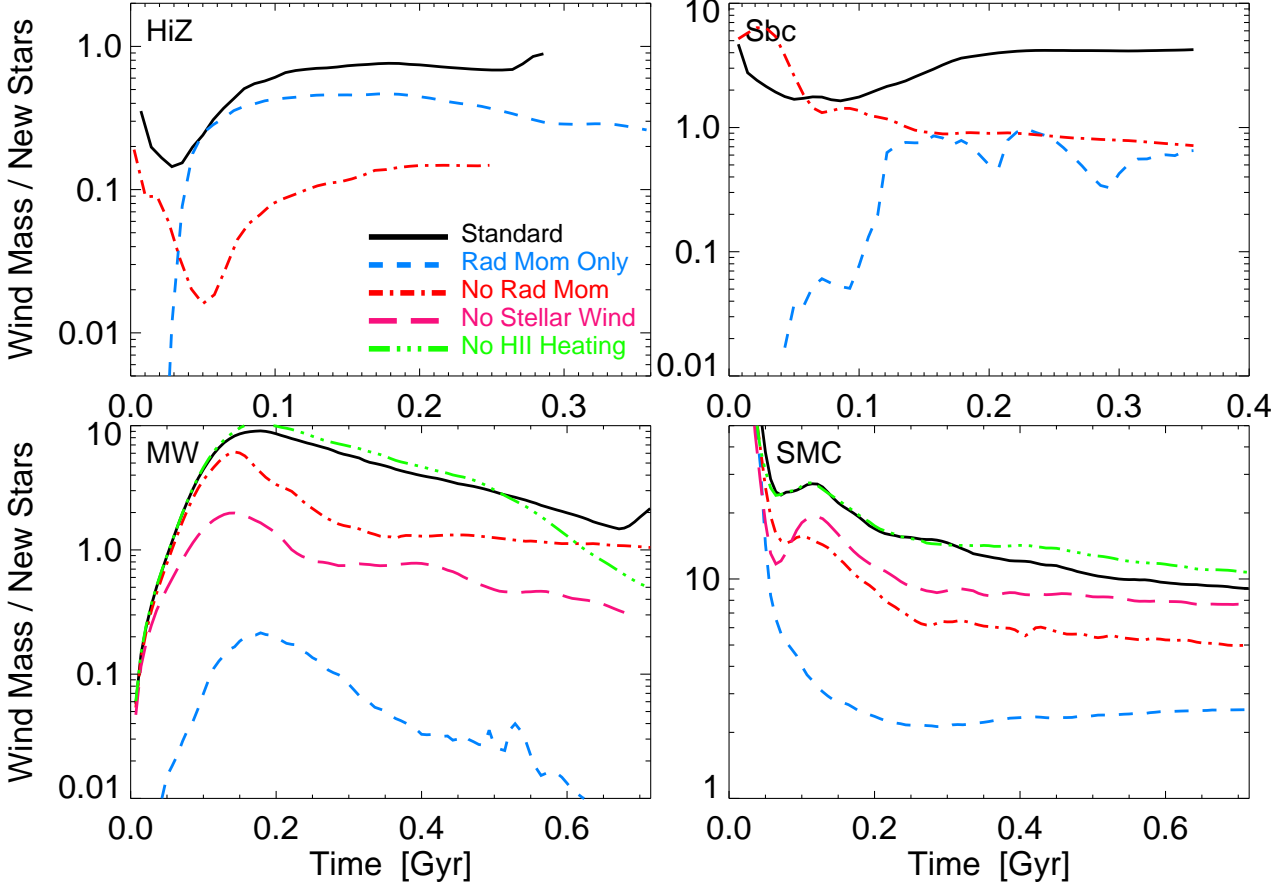


Figure 6. Galactic wind mass-loading efficiency ($\equiv M_{\text{wind}}/M_{\text{new}}$; where $M_{\text{wind}} = \int \dot{M}_{\text{wind}}$ and $M_{\text{new}} = \int \dot{M}_*$) for each galaxy model. We compare our standard simulations with all feedback mechanisms to simulations with different feedback mechanisms enabled in turn. Models with no feedback produce no measurable wind mass. Since SNe dominate the production of wind material by hot gas (relative to HII heating and stellar winds), the “Rad Mom Only” models shown here are very similar to “no SNe” models. *Top Left:* HiZ model. Net outflow rate is $\sim \dot{M}_*$. Most of the wind comes from “cold” acceleration by radiation pressure, and is present even with no SNe/stellar wind/HII heating terms (though these do contribute a non-negligible fraction from “venting,” seen in the no radiation pressure case). *Top Right:* Sbc model, with $\dot{M}_{\text{wind}} \sim 3 - 5 \dot{M}_*$. Heating mechanisms contribute comparably to radiation pressure in driving the wind. Note that the “standard” model wind mass is significantly larger than the sum of the wind mass with just heating and just radiation pressure enabled separately – there is a strong non-linear coupling between the different feedback mechanisms that enhances the strength of the wind. *Bottom Left:* MW-like model, with $\dot{M}_{\text{wind}} \sim 1 - 10 \dot{M}_*$. Here the hot gas produced by SNe dominates the wind driving. *Bottom Right:* SMC-like model, with $\dot{M}_{\text{wind}} \sim 10 - 20 \dot{M}_*$. Hot gas is again critical, with SNe even more dominant.

regions), there is essentially no wind! And of the heating mechanisms, SNe have the largest effect on the wind properties. Absent thermal heating, the SFR is still regulated at nearly the same level by the radiation pressure feedback (as in Paper I), but material is not being driven into a super-wind. Radiation pressure thus plays an important role in self-regulating star formation in the disk, but is not, unlike in the HiZ models, strong enough to directly accelerate much gas far out of the disk. Rather, radiation pressure lifts material out of GMCs, after which the gas is accelerated primarily by the hot gas pressure into a galaxy-scale outflow. This contrasts with the HiZ case, where the acceleration above the disk results from radiation pressure rather than from hot gas ram pressure.

The Sbc case, as before, lies somewhere in between the HiZ and MW cases. The net efficiency is a few times the SFR, with radiation pressure and hot gas contributing comparably to the outflow mass. Note also that Figure 6 clearly shows that the total wind mass in the case with all feedback enabled (“standard”) is significantly larger than the sum of the wind mass with hot gas alone or radiation pressure alone. The full wind efficiency stems from the non-linear interaction between different feedback mechanisms.

For our SMC-like dwarf galaxy model, the simulation with all feedback mechanisms included drives an outflow of $\sim 10 - 20$ times the SFR (Fig. 6). Just as in the MW model, SNe are the most important driver of the galactic outflow. In particular if we remove all sources of hot gas (SNe and stellar winds), we again see essentially no significant super-wind. By contrast, without any feedback from radiation pressure, the wind mass is reduced by a small amount ($\sim 30 - 40\%$) and the average SFR increases by a similar factor, so the net outflow efficiency is only a factor ~ 1.7 lower.

4.2 Wind Efficiency versus Galaxy Mass

Figure 7 summarizes the efficiency of the winds in our standard simulations as a function of global galaxy properties. We plot the wind efficiency at several different times (evaluated every 10^7 yr), for each standard disk model, as a function of several parameters: the instantaneous SFR, the maximum circular velocity of the disk V_{max} , and the stellar and baryonic galaxy masses. The order-of-magnitude scatter in wind efficiencies even at fixed galaxy proper-

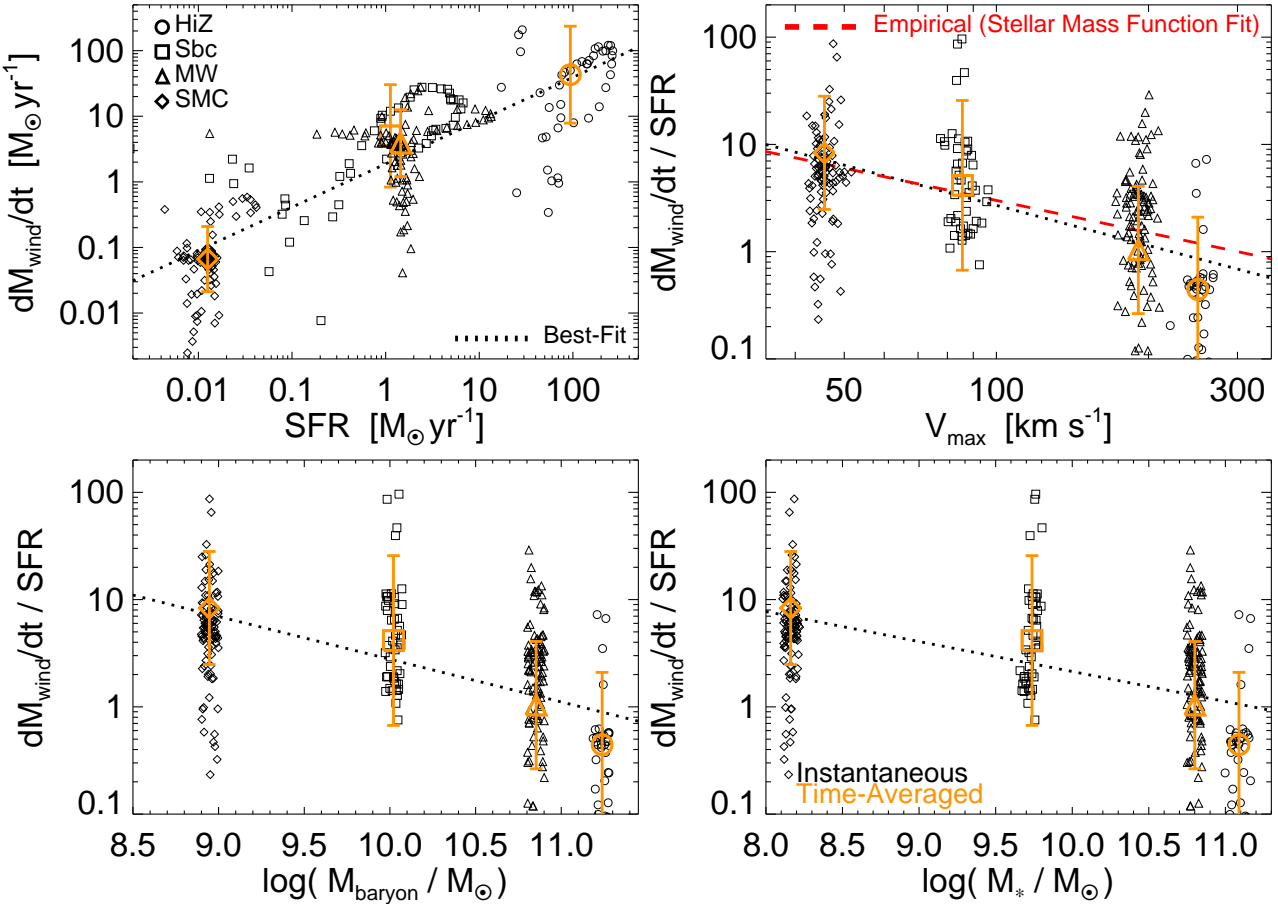


Figure 7. Summary of the efficiency of stellar winds, defined as the wind mass loss rate divided by the SFR, $\dot{M}_{\text{wind}}/\dot{M}_*$. Each of our galaxy models is shown, for simulations with all feedback mechanisms included. The instantaneous efficiencies (the derivative of Fig. 6) are shown at a number of times (black); the time-averaged value and $\pm 1\sigma$ scatter over the duration of the simulation is also shown (orange with error bars). The best-fit power-law relation is also plotted in each panel (dotted line). *Top Left:* Outflow rate versus SFR. The best-fit is sub-linear: $\dot{M}_{\text{wind}} \propto \dot{M}_*^{0.66 \pm 0.08}$ (eq. 3). *Top Right:* Efficiency versus the maximum circular velocity of the galaxy rotation curve. Our best-fit is $\dot{M}_{\text{wind}}/\dot{M}_* \propto V_{\text{max}}^{1.2 \pm 0.2}$ (eq. 4). For comparison, we also show the scaling from cosmological simulations that are adjusted to match high-redshift IGM enrichment and approximately match the observed galaxy mass function (Oppenheimer & Davé 2006; Oppenheimer et al. 2010):⁶ $\langle \dot{M}_{\text{wind}}/\dot{M}_* \rangle = (V_{\text{max}}/300 \text{ km s}^{-1})^{-1}$ (red dashed). This is consistent within 1σ with our numerical results. *Bottom Left:* Wind efficiency versus galaxy baryonic mass. *Bottom Right:* Wind efficiency versus galaxy stellar mass.

ties is clear, but there are also clear trends in the average efficiencies with each galaxy property.

The wind mass loading is strongly correlated with the galaxy SFR, but with a sub-linear power. Fitting a single power-law in Figure 7 gives

$$\dot{M}_{\text{wind}} \sim 3 M_\odot \text{ yr}^{-1} \left(\frac{\dot{M}_*}{M_\odot \text{ yr}^{-1}} \right)^{0.7} \quad (3)$$

The sub-linear behavior is particularly interesting, as it implies a lower efficiency at higher absolute SFR: $\dot{M}_{\text{wind}}/\dot{M}_* \propto \dot{M}_*^{-0.3}$. Since observations find a SFR-stellar mass relation $\dot{M}_* \propto M_*^{0.7}$ in star-forming systems (Noeske et al. 2007), this is equivalent to a lower efficiency at higher masses ($\dot{M}_{\text{wind}}/\dot{M}_* \propto M_*^{-0.23}$).

This is evident when we directly plot the efficiency versus baryonic mass, stellar mass, or maximum circular velocity. The strongest correlation appears to be between efficiency and V_{max} . This has the form

$$\left\langle \frac{\dot{M}_{\text{wind}}}{\dot{M}_*} \right\rangle \sim 3[\pm 1] \left(\frac{V_{\text{max}}}{100 \text{ km s}^{-1}} \right)^{-(0.9-1.7)}. \quad (4)$$

This is in reasonable agreement with the expectation from simple

dimensional arguments based for a momentum-driven wind with a characteristic velocity of V_{max} (Murray et al. 2005). If the momentum flux in the outflow scales with the luminosity of massive stars ($\propto L \propto \dot{M}_*$), then the outward momentum $\dot{M}_{\text{wind}} V_{\text{esc}} \propto \dot{M}_*$, so $\dot{M}_{\text{wind}}/\dot{M}_* \propto V_{\text{max}}^{-1}$. Note that this scaling can also apply if ram pressure due to hot gas is the primary mechanism driving mass (i.e., warm/cold gas) out of the galaxy.⁵ There is a small, but real deviation of the HiZ model from the extrapolation of this scaling, which is a consequence of an additional residual dependence on Σ_{gas} that we discuss below.

The scaling of $\dot{M}_{\text{wind}}/\dot{M}_*$ with V_{max} in Figure 7 and equation 4 is in plausible agreement with the scaling suggested in cosmological simulations in order to produce a good match between the predicted and observed galaxy stellar (and baryonic) mass functions as well as high-redshift IGM enrichment patterns. Oppenheimer & Davé (2006) and Oppenheimer et al. (2010) (see

⁵ We should note that, although it is not obvious because of the large scatter in instantaneous mass-loading rates, the best-fit trend in Figure 7 is robust to the exclusion of any individual simulation.

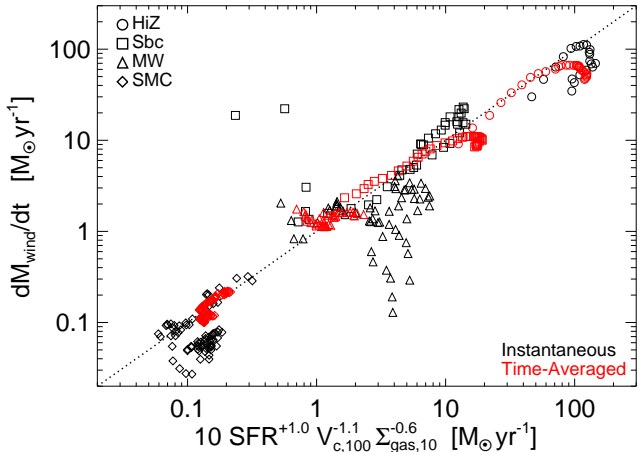


Figure 8. Best-fit scaling of the wind mass rate as a function of galaxy properties in our numerical simulations (eq. 8): roughly $\dot{M}_{\text{wind}}/\dot{M}_* \propto V_c^{-1} \Sigma_{\text{gas}}^{-1/2}$ (where the quantities are evaluated at each wind launching radius R in the galaxy). The dotted line shows the identical relation. Black points show the instantaneous efficiencies (as Fig. 7), red points the running time-average (as Fig. 6, with quantities evaluated at the half-SFR radius at each time). The order-of-magnitude scatter in Fig. 7 is reduced to factor ~ 2 . The scaling $\dot{M}_{\text{wind}}/\dot{M}_* \propto \Sigma_{\text{gas}}^{-1/2}$ reflects the fact that in denser systems, SNe cool more efficiently and more of the optical/UV radiation is absorbed, reducing the efficiency of wind driving.

also Dutton & van den Bosch 2009) considered a series of prescriptions for how galactic winds scale with galaxy properties, and ultimately found agreement with observations for a scaling $\dot{M}_{\text{wind}}/\dot{M}_* = 3(V_{\text{max}}/100 \text{ km s}^{-1})^{-1}$, which lies in the best-fit range of our simulations (as shown by the red line in Fig. 7).⁶ We stress that we have not tuned or adjusted any parameters in our simulations to produce either the normalization or slope of this relation.

Qualitatively similar behavior appears when we consider the wind efficiency versus baryonic or stellar mass, albeit with a slightly less significant correlation.

$$\left\langle \frac{\dot{M}_{\text{wind}}}{\dot{M}_*} \right\rangle \sim 3.5[\pm 1] \left(\frac{M_{\text{baryon}}}{10^{10} M_\odot} \right)^{-(0.3-0.65)} \quad (5)$$

$$\left\langle \frac{\dot{M}_{\text{wind}}}{\dot{M}_*} \right\rangle \sim 2[\pm 0.5] \left(\frac{M_*}{10^{10} M_\odot} \right)^{-(0.25-0.5)}. \quad (6)$$

Given the observed (stellar and baryonic) Tully-Fisher relation $M_* \propto V_{\text{max}}^4$; these correlations are fully consistent with the V_{max} correlation; likewise given the $\dot{M}_* - M_*$ relation discussed above, these are consistent with the wind mass-SFR relation. This consistency is expected, given that the simulated galaxies lie on both the observed Tully-Fisher relations (by design) and SFR-stellar mass relation.

⁶ Oppenheimer & Davé (2006); Oppenheimer et al. (2010) actually do not resolve V_{max} and instead adopt a proxy for the velocity dispersion σ based on a galaxy mass estimated from a friends-of-friends object finder. Without a matching cosmological simulation, it is difficult to exactly convert between this and the quantities measured here, so there is some ambiguity in whether the normalization estimated in the quoted values agrees exactly with that implemented. The scaling with V_{max}^{-1} , however, should be more robust.

4.3 Predicting Wind Efficiencies: Towards a More Accurate Effective Model

In this section we use the results of our simulations to assess if there is a more accurate predictor of wind properties than equations 3-6 – such a predictor would be extremely useful for application in cosmological simulations and/or semi-analytic models.

First, we consider the simulations alone, including all of our galaxy models and case studies where we have varied other parameters such as the galaxy structural properties and how the SFR is tied to molecular gas. We isolate a series of properties that are measurable in such models (each as a function of radius): SFR, circular velocity, escape velocity, total/bulge/disk/gas/halo masses and surface densities, scale-heights, and the radii themselves (most other properties can be constructed from combinations of these). We then compare to the corresponding instantaneous wind mass loading $\dot{M}_{\text{wind}}(R, t)$. Although all the parameters are correlated, if we marginalize over the other variables we find three parameters that dominate the trends in \dot{M}_{wind} with radius, time, and galaxy model: the SFR \dot{M}_* , circular velocity⁷ V_c , and gas surface density Σ_{gas} . Accounting for these, we do not find $> 3\sigma$ dependence on any other variables we consider. A maximum-likelihood fit to these three variables gives a correlation of the form

$$\dot{M}_{\text{wind}} \propto \dot{M}_*^\alpha V_c^\beta \Sigma_{\text{gas}}^\gamma \quad (7)$$

with $\alpha \approx 1.0 \pm 0.15$, $\beta \approx -1.1 \pm 0.25$, and $\gamma \approx -0.5 \pm 0.15$. From this, the correlation with SFR is most significant ($> 5\sigma$), and at otherwise fixed properties scales linearly ($\dot{M}_{\text{wind}} \propto \dot{M}_*$); the sub-linear behavior in Fig. 7 owes mostly to the next most-significant correlation, with $V_c(R, t)$ ($\sim 4\sigma$), which is consistent with the expected $\propto V_c^{-1}$. Third most important (but still $> 3\sigma$) is a residual correlation with surface density which dominates many of the variations in $\dot{M}_{\text{wind}}/\dot{M}_*$ within a given model as a function of radius and time. If we include the normalization in the fit, we find the following result for the mass loading

$$\left\langle \frac{\dot{M}_{\text{wind}}}{\dot{M}_*} \right\rangle_R \approx 10 \eta_1 \left(\frac{V_c(R)}{100 \text{ km s}^{-1}} \right)^{-(1+\eta_2)} \left(\frac{\Sigma_{\text{gas}}(R)}{10 M_\odot \text{ pc}^{-2}} \right)^{-(0.5+\eta_3)} \quad (8)$$

where η_1, η_2, η_3 incorporate the uncertainty from the fits ($\eta_1 \sim 0.7 - 1.5$, $\eta_2 \sim \pm 0.3$, $\eta_3 \sim \pm 0.15$). A comparison between this fit and the simulation results is shown in Figure 8.

Note that the scalings with star formation rate and circular velocity in equation 7 are consistent with the simple momentum conservation argument discussed after equation 4. The surface density scaling is, however, new. It implies that the wind mass loading is lower for higher gas surface density systems, all other things being equal. Physically, our interpretation of this is as follows. First, consider low mass systems where SNe dominate the wind driving. As shock-heated SN bubbles expand, the momentum of the swept-up material increases in time due to the P-dV work done by the hot gas. This enhances the wind driving so long as cooling does not sap the energy of the SN bubbles. For higher surface density galaxies, however, radiative cooling of SN remnants is more important, suppressing the SNe contribution to the wind. This is qualitatively consistent with the scaling in equation 8.

Consider now the opposite limit of massive, dense systems in which radiation pressure is the most important wind driving mechanism in our models, in particular the long-range continuous acceleration due to the diffuse radiation field. The gas at large heights

⁷ Because we are considering the winds at different galactic radii $\dot{M}_{\text{wind}}(R, t)$, we use $V_c(R)$ instead of $V_{\text{max}} \equiv \text{MAX}(V_c[R])$.

above the midplane is generally not optically thick in the IR, but still has $\tau > 1$ in the UV (and possibly in the optical, if the wind is sufficiently dense). Thus the incident radiation pressure force on this gas depends on the escape fraction in the UV/optical $f_{\text{esc, uv-opt}}$ times L/c , so that $\dot{M}_{\text{wind}} \propto f_{\text{esc, uv-opt}} \dot{M}_* V_c^{-1}$. In the Appendix, we explicitly confirm that the wind mass-loading in the HiZ and Sbc models indeed scales close to linearly with $f_{\text{esc, uv-opt}}$. The escape fraction in turn declines for larger disk gas surface densities, because the disk is itself what is absorbing the UV flux. This implies a wind mass-loading that decreases for higher gas surface densities, again qualitatively consistent with the scaling in equation 8.

5 DISCUSSION

We have studied the origin of galaxy-scale outflows using a new set of numerical methods for modeling stellar feedback in hydrodynamic galaxy simulations; the feedback processes include radiation pressure on the scales of star clusters; shock-heating, momentum injection, and gas recycling via supernovae and stellar winds; photo-ionization in (overlapping) HII regions; and radiation pressure produced by the diffuse interstellar radiation field. Our calculations use the results of stellar population modeling to self-consistently include the time-dependence of these feedback processes. We have explored this physics in the context of isolated (non-cosmological) galaxy models that range from those motivated by massive $z \sim 2$ galaxies forming stars at $\sim 100 - 300 M_\odot \text{ yr}^{-1}$ to models of SMC-like dwarf galaxies.

By incorporating multiple feedback processes, we find that numerical simulations produce galaxy-scale outflows with mass loading factors up to $\dot{M}_{\text{wind}} \gtrsim 10 \dot{M}_*$. Moreover, the wind mass-loading is the largest in the lowest mass galaxies, scaling approximately as $\sim V_c^{-1}$ (although with an additional gas surface density dependence that we discuss below). This is, to our knowledge, the first time that hydrodynamic simulations have demonstrated that stellar feedback processes can self-consistently generate galactic winds with *sufficiently large mass-loading and the appropriate galaxy mass-dependence* to match what has been invoked to explain the shape of the the galaxy stellar mass function.

A general feature of our results is that the interaction between multiple feedback processes, acting on different spatial and temporal scales, is important for driving realistic galactic winds. In particular, some feedback processes prevent runaway collapse within GMCs, thus maintaining a diffuse phase of the ISM that is more susceptible to feedback. In general a different set of processes then accelerates the wind material out of the star-forming disk.

By turning off individual processes in our numerical simulations, we can identify the mechanisms responsible for most of the wind mass-loading in a given galaxy model. In dense gas, typical of high-redshift rapidly star-forming galaxies (our HiZ model) and local starburst galaxies (local LIRGs and dense nuclei such as Arp 220), cooling times even in the “diffuse” ISM are extremely short, and thus energy input into the ISM by SNe and stellar winds is rapidly radiated away. This heating can neither halt the runaway collapse of massive GMC complexes or accelerate significant amounts of material into a wind (since most of the gas is in the dense medium). Instead, radiation pressure from trapped IR photons in star-forming regions serves to dissociate those regions, and “lifts up” gas above the disk – there, the gas “feels” the coherent momentum flux from the optical/UV/IR photons escaping the other star clusters in the disk, and can be continuously accelerated out of the galaxy. Most of the wind mass in our models of these dense

systems is in cold, dense blobs radiatively accelerated out of the galaxy; the small amount of hot gas is volume filling but has little mass, and is too tenuous to significantly accelerate the dense material. Under these conditions, we find that the net wind efficiencies are typically moderate, $\dot{M}_{\text{wind}} \sim 0.1 - 2 \dot{M}_*$.

In lower-gas density systems such as the MW and dwarf starbursts such as M82 (analogous to our Sbc model) ($\langle n \rangle \sim 1 \text{ cm}^{-3}$), heating mechanisms and direct momentum injection have comparable effects. Injection of momentum by radiation pressure, O-star winds, and photo-heating when stars clusters have ages $< 10^6 \text{ yr}$ begins to dissociate their host GMCs and punch holes that allow SNe remnants to expand and escape into the diffuse/hot medium. There, cooling times are low, and bubbles can grow, overlap, and do PdV work on the entrained warm and cold gas, contributing significantly to the wind driving. With all feedback mechanisms included, dwarf starbursts generate galactic winds with mass-outflow rates $\sim 2 - 5$ times the SFR.

In our dwarf galaxy model (motivated by the SMC), and in the outer extended disks of more massive systems, the gas densities are very low ($\langle n \rangle \lesssim 0.1 \text{ cm}^{-3}$). The cooling time can be comparable to or longer than the dynamical time so that heating mechanisms become very efficient; such systems also have low stellar surface densities and gas optical depths, so radiation pressure is less important. A combination of momentum from UV photons, stellar winds, and warm gas pressure from photo-ionized regions stirs up star-forming regions, allowing SNe explosions to expand rapidly and generate large, overlapping hot bubbles. This generates a characteristic dwarf irregular morphology with patchy star-forming regions and hot SNe bubbles (see also Governato et al. 2010). These hot bubbles push cold shells and loops into a super-wind as they overlap, generating a multi-phase (mostly hot/warm) wind with a large mass loss rate $\dot{M}_{\text{wind}} \sim 10 - 20 \dot{M}_*$. Without SNe, there is still some hot gas and a “bubble-like” morphology driven by high velocity stellar (O-star) winds, but SFRs are a factor $\gtrsim 5$ larger and (absolute) mass outflow rates a factor of ~ 20 lower.

We have used our simulations to determine improved prescriptions for wind mass-loss rates (eq. 8) and velocity distributions (eq 2) for use in cosmological simulations and semi-analytic models of galaxy evolution (for which the explicit models here cannot yet be implemented): $\dot{M}_{\text{wind}}/\dot{M}_* \propto V_c^{-1} \Sigma_{\text{gas}}^{-1/2}$. This fit is similar to what has been adopted phenomenologically in the past, but incorporates an additional correction such that the mass-loading decreases with increasing gas surface density $\propto \Sigma_{\text{gas}}^{-0.5}$ (at fixed circular velocity). In the radiation-pressure dominated regime, this reflects the fact that a dense disk captures more of the primary stellar luminosity very close to stars, downgrading photons into the IR. These degraded photons can help drive turbulence in very dense regions (with $\tau_{\text{IR}} \gg 1$) but generally do not contribute to accelerating material above the disk. In the SNe-dominated regime, the surface density scaling reflects the fact that more of the SN energy is radiated away in denser systems.

In addition to introducing variations between galaxies with the same V_c , the Σ_{gas} dependence will introduce some additional systematic scaling with mass and circular velocity. At fixed redshift, total disk surface density tends to increase with mass and V_c , but at intermediate masses ($M_* \gtrsim 10^{10} M_\odot$) gas fractions also decline with mass such that Σ_{gas} (measured within the star-forming disk, which is the important scale for winds) is nearly independent of galaxy mass (e.g. McGaugh 2005; Hall et al. 2011). At lower masses, however, where $M_{\text{gas}} \gtrsim M_*$, Σ_{gas} scales with mass as $\sim V_c^{1-2}$, steepening the mass-loading by an additional power of V_c . This may resolve some of the problems noted in Davé et al. (2011),

where a simpler single power-law scalings tends to over-produce the number of low-mass galaxies.

The scaling we have inferred for the mass loss rate is applicable to a range of galaxies but may break down in two different extremes, which we will explore in future work. In the lowest mass dwarf galaxies (with $M_* \lesssim 10^6 M_\odot$ and $Z \ll 0.01 Z_\odot$), the ionizing background alone may be sufficient to suppress most structure, metallicities may be sufficiently low as to prevent molecule formation except under extreme conditions, and a single SNe can clear out the gas supply; our simulations do not apply to these circumstances. At the opposite extreme, in the most dense regions of nuclear starbursts and material surrounding AGN, even the “diffuse” medium can be optically thick in the IR and many of our assumptions about the efficiency of radiation pressure and the (in)ability of IR photons to drive winds are likely to be modified.

We also caution that care is needed when mapping the scaling here – which assumes the disk structure is marginally resolved and so quantities like V_c and Σ can be evaluated at the effective radius of star formation – to models with poor resolution. For example, in the Oppenheimer & Davé (2006) cosmological simulations (and many analytic models), R_{disk} and $V_c(R_{\text{disk}})$ are unresolved, so they are implicitly assumed to scale in a simple manner with total galaxy baryonic mass (and redshift). If we use the observed Tully-Fisher relation and gas fraction-stellar mass relations as noted above to convert our proposed scaling to a strict power of mass and redshift, the scalings are similar at intermediate masses. But it is in general non-trivial to link the quantities relevant to the outflows in our simulations (e.g., Fig. 8) to global parameters like halo/baryonic mass or halo circular velocity.

The calculations presented in this paper can clearly be improved in a number of ways in future work. Most notably our treatment of the radiation pressure produced by UV, optical, and IR photons is quite approximate. A full calculation including the scattering and absorption of both the UV and IR photons is technically formidable. We have calibrated our treatment of the diffuse radiation field in galaxies using such radiative transfer calculations (Paper II) but additional improvements to our methods would be valuable. Our calculations also do not include cosmic-rays generated in SN shocks, which empirically contribute significantly to the pressure-support of MW-like spiral galaxies (Boulares & Cox 1990) and may also contribute significantly to driving outflows from such galaxies. And we reiterate that even at our highest resolution, there are important numerical caveats (and unresolved mixing processes) that may apply to the phase structure of the winds.

Finally, our calculations have focused on idealized, isolated galaxy models and do not include a realistic hot coronal gas component, galactic inflow, or an external intergalactic medium. The interaction between galactic outflows, hot halo gas, and inflowing cold streams is an extremely interesting problem that should be studied in detail in future work. Because we have not captured this interaction, the outflow rates we calculate are best interpreted as outflow rates from the star-forming disk, rather than from the virial radius of the host dark matter halo.

ACKNOWLEDGMENTS

We thank Todd Thompson and Romeel Davé for helpful discussions. Support for PFH was provided by the Miller Institute for Basic Research in Science, University of California Berkeley. EQ is supported in part by NASA grant NNG06GI68G and the David and Lucile Packard Foundation. NM is supported in part by

NSERC and by the Canada Research Chairs program.

REFERENCES

- Aguirre, A., Hernquist, L., Schaye, J., Weinberg, D. H., Katz, N., & Gardner, J. 2001, ApJ, 560, 599
- Boulares, A., & Cox, D. P. 1990, ApJ, 365, 544
- Brook, C. B., et al. 2011, MNRAS, 415, 1051
- Chen, Y.-M., Tremonti, C. A., Heckman, T. M., Kauffmann, G., Weiner, B. J., Brinchmann, J., & Wang, J. 2010, AJ, 140, 445
- Cole, A. L., Weiner, B. J., Holz, D. E., Cooper, M. C., Yan, R., & Aird, J. 2011, ApJ, 743, 46
- Cole, S., Lacey, C. G., Baugh, C. M., & Frenk, C. S. 2000, MNRAS, 319, 168
- Davé, R., Oppenheimer, B. D., & Finlator, K. 2011, MNRAS, 415, 11
- Dutton, A. A., & van den Bosch, F. C. 2009, MNRAS, 396, 141
- Erb, D. K., Shapley, A. E., Pettini, M., Steidel, C. C., Reddy, N. A., & Adelberger, K. L. 2006, ApJ, 644, 813
- Evans, N. J., et al. 2009, ApJS, 181, 321
- Evans, II, N. J. 1999, ARA&A, 37, 311
- Genel, S., et al. 2012, ApJ, 745, 11
- Governato, F., et al. 2007, MNRAS, 374, 1479
- . 2010, Nature, 463, 203
- Guo, Q., White, S., Li, C., & Boylan-Kolchin, M. 2010, MNRAS, 404, 1111
- Hall, M., Courteau, S., Dutton, A. A., McDonald, M., & Zhu, Y. 2011, MNRAS, in press [arXiv:1111.5009]
- Heckman, T. M., Lehnert, M. D., Strickland, D. K., & Armus, L. 2000, ApJS, 129, 493
- Hernquist, L. 1990, ApJ, 356, 359
- Hopkins, P. F., Hernquist, L., Martini, P., Cox, T. J., Robertson, B., Di Matteo, T., & Springel, V. 2005, ApJL, 625, L71
- Hopkins, P. F., Quataert, E., & Murray, N. 2011, MNRAS, 417, 950
- . 2012, MNRAS, 421, 3488
- Katz, N., Weinberg, D. H., & Hernquist, L. 1996, ApJS, 105, 19
- Kennicutt, Jr., R. C. 1998, ApJ, 498, 541
- Keres, D., Vogelsberger, M., Springel, V., & Hernquist, L. 2011, in AAS Meeting Abstracts #218, 119.02–+
- Kereš, D., Katz, N., Davé, R., Fardal, M., & Weinberg, D. H. 2009a, MNRAS, 396, 2332
- . 2009b, MNRAS, 396, 2332
- Kroupa, P. 2002, Science, 295, 82
- Krumholz, M. R., & Gnedin, N. Y. 2011, ApJ, 729, 36
- Krumholz, M. R., & Tan, J. C. 2007, ApJ, 654, 304
- Leitherer, C., et al. 1999, ApJS, 123, 3
- Mannucci, F., Della Valle, M., & Panagia, N. 2006, MNRAS, 370, 773
- Martin, C. L. 1999, ApJ, 513, 156
- . 2005, ApJ, 621, 227
- . 2006, ApJ, 647, 222
- McGaugh, S. S. 2005, ApJ, 632, 859
- Murray, N., Ménard, B., & Thompson, T. A. 2011, ApJ, 735, 66
- Murray, N., Quataert, E., & Thompson, T. A. 2005, ApJ, 618, 569
- Nagamine, K. 2010, Advances in Astronomy, 2010
- Newman, S. F., et al. 2012, ApJ, in press, arXiv:1204.4727
- Noeske, K. G., et al. 2007, ApJL, 660, L43
- Oppenheimer, B. D., & Davé, R. 2006, MNRAS, 373, 1265
- . 2008, MNRAS, 387, 577
- Oppenheimer, B. D., Davé, R., Kereš, D., Fardal, M., Katz, N., Kollmeier, J. A., & Weinberg, D. H. 2010, MNRAS, 406, 2325

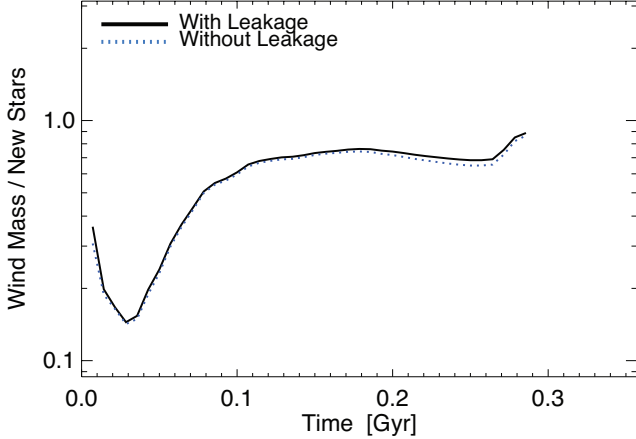


Figure A1. Effects of allowing for photon “leakage” – i.e. assuming that the ISM is clumpy and porous on sub-resolution scales. We plot the wind mass-loading versus time (as Figure 6) for an otherwise identical standard HiZ simulation. Our standard model (“without leakage”) takes the local column density estimator as-is, and estimates the escape fraction from the spectrum of each star with $f_{\text{esc}} = \exp(-\tau)$ for each waveband. The “with leakage” model assumes that each star is actually surrounded by an (unresolved) distribution of columns following a power-law distribution (see Paper I for details) and uses this to calculate f_{esc} . The allowance for leakage only makes a difference when the average opacity is large, at which point the contribution (in either case) to the global total luminosity in the relevant band is small. As a result it has a negligible effect on our results.

- Pettini, M., Madau, P., Bolte, M., Prochaska, J. X., Ellison, S. L., & Fan, X. 2003, ApJ, 594, 695
 Powell, L. C., Slyz, A., & Devriendt, J. 2011, MNRAS, 414, 3671
 Rupke, D. S., Veilleux, S., & Sanders, D. B. 2005, ApJ, 632, 751
 Sales, L. V., Navarro, J. F., Schaye, J., Vecchia, C. D., Springel, V., & Booth, C. M. 2010, MNRAS, 409, 1541
 Sato, T., Martin, C. L., Noeske, K. G., Koo, D. C., & Lotz, J. M. 2009, ApJ, 696, 214
 Somerville, R. S., & Primack, J. R. 1999, MNRAS, 310, 1087
 Songaila, A. 2005, AJ, 130, 1996
 Springel, V. 2005, MNRAS, 364, 1105
 Springel, V. 2010, MNRAS, 401, 791
 Springel, V., & Hernquist, L. 2003a, MNRAS, 339, 289
 —. 2003b, MNRAS, 339, 312
 Steidel, C. C., Erb, D. K., Shapley, A. E., Pettini, M., Reddy, N., Bogosavljević, M., Rudie, G. C., & Rakic, O. 2010, ApJ, 717, 289
 Thacker, R. J., & Couchman, H. M. P. 2000, ApJ, 545, 728
 Tremonti, C. A., et al. 2004, ApJ, 613, 898
 Weiner, B. J., et al. 2009, ApJ, 692, 187
 White, S. D. M., & Frenk, C. S. 1991, ApJ, 379, 52
 Wiersma, R. P. C., Schaye, J., & Smith, B. D. 2009, MNRAS, 393, 99
 Williams, J. P., & McKee, C. F. 1997, ApJ, 476, 166
 Zuckerman, B., & Evans, II, N. J. 1974, ApJL, 192, L149

APPENDIX A: NUMERICAL TESTS

Extensive numerical tests of the models used here are presented in Paper I and Paper II. We refer to those papers for details, but briefly summarize the results of those numerical tests for galactic winds.

In Paper I, we note that the ISM is probably inhomogeneous

below our resolution scale, which can allow photons to “leak out” from the region around their parent star at a rate higher than the nominal $\exp(-\tau_0)$ which we use to attenuate the spectrum when calculating the radiation pressure effects. This will weaken the short-range radiation pressure, but strengthen the long-range radiation pressure forces (since more short-wavelength photons escape, to which the “diffuse” medium has a higher optical depth). In Paper I and Paper II, we show that the “escape fraction” (and hence modification to these forces) is straightforward to calculate analytically, if we assume some *a priori* functional form for the sub-grid local density distribution. In Figure A1, we show the consequences for the winds if we replace our usual estimator of local attenuation, $f_{\text{esc}} = \exp(-\tau_0)$, with the appropriately modified f_{esc} assuming that a gas particle with mean opacity τ_0 really represents a complete distribution of opacities with that median but a power-law functional form and dispersion of ≈ 0.6 dex (chosen to match the median from higher-resolution simulations of sub-regions). We test this for the HiZ model, since this is the model most sensitive to the radiation pressure effects. Adopting a lognormal distribution gives a nearly identical result, for all dispersions $\approx 0 - 2$ dex (see Paper I). In Paper I we showed our treatment of the subgrid escape fraction had little effect on the SFR. Here, we see that it also has no significant effect on the resulting galactic wind. The reason is that for low/intermediate τ_0 , the escape fractions are large (and hence similar) regardless of sub-structure; for high τ_0 the escape fractions can be very different, but they are both still small and contribute negligibly to the total coupled momentum.

In Paper II, we note that we can isolate the effects of the emergent galaxy SED shape on the winds by comparing our full model (in which the emergent flux from each star particle in the UV/optical/IR is estimated from the stellar age and local attenuation) to one in which we simply set the SED shape by hand and force it to be the same for all particles. Specifically, we calculate the bolometric luminosity and incident force on all gas particles in our standard fashion, but simply force the values $L_{\text{UV}}/L_{\text{bol}}$, $L_{\text{Opt}}/L_{\text{bol}}$, $L_{\text{IR}}/L_{\text{bol}}$ to equal some chosen values.

Figure A2 compares our standard model, for each galaxy type, to two choices for this “enforced SED” model. First, we consider a model in which the SED shape is chosen for each galaxy model to match observations of galaxies with similar stellar mass, SFR, and redshift. The observations are discussed in Paper II, but for typical observational counterparts to each of our galaxy models, $(f_{\text{UV}}, f_{\text{Opt}}, f_{\text{IR}})$ is approximately equal to $(0.05, 0.2, 0.75)$ for the HiZ, $(0.13, 0.40, 0.47)$ for the MW, $(0.3, 0.3, 0.4)$ for the SMC, and $(0.07, 0.23, 0.7)$ for the Sbc models. There is substantial scatter in otherwise similar galaxies and uncertainty in these quantities, but they provide an approximate guide. Reassuringly, the resulting wind masses are quite similar to our “standard model,” so it is likely that the simulations are capturing the key physics of radiative acceleration despite lacking a complete on-the-fly radiation hydrodynamics. This is consistent with the fact that in Paper II we showed that the predicted SEDs from our radiation pressure model are similar to those observed.

We also show in Figure A2 the wind mass-loading if we were to assume a uniform SED shape with a significantly higher UV/optical escape fraction. For all models, this serves to substantially enhance the coupled momentum for material above the disk and so enhances the wind mass (and suppresses the SFR, shown in Paper II). This confirms two important points discussed in the text. First, on large scales (as opposed to e.g. inside GMCs) the gas is optically thin in the IR, and so it is the UV/optical photons that dominate the long-range radiative acceleration of winds. Second,

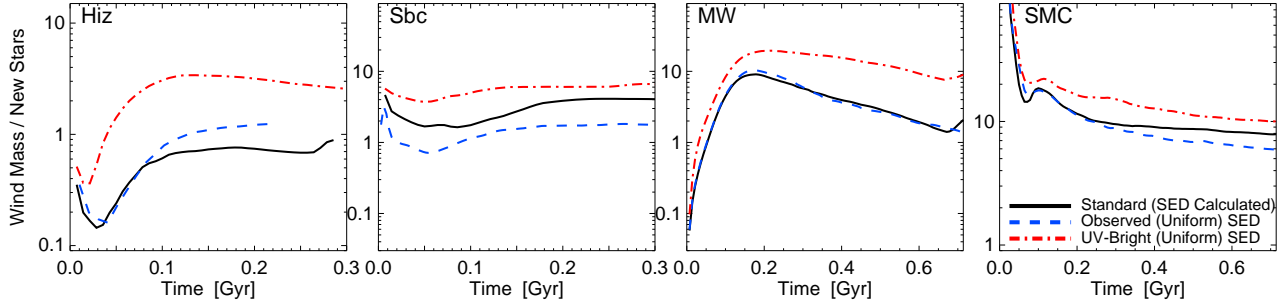


Figure A2. Comparison of our standard long-range radiation pressure model (where the attenuation and SED shape of each star particle is calculated) to one in which we simply force the SED shape to match a specific empirical template. We show the resulting wind mass-loading versus time (as Figure 6) for each of the HiZ/Sbc/MW/SMC models. In each, we compare our standard model (black) in which the SED shapes are self-consistently calculated on-the-fly, to a model where the SED shape (L_{bol} is still determined self-consistently) is forced to a constant fixed value chosen to match the observed mean SED shape for similar observed galaxies to each model (blue). These choices amount to a relative proportion of L_{bol} in the UV/optical/IR bands of (0.05, 0.15, 0.8), (0.07, 0.23, 0.7), (0.1, 0.4, 0.5), (0.2, 0.3, 0.5) for the HiZ/Sbc/MW/SMC cases. In each case, the self-consistent and empirically fixed models give SFRs in reasonable agreement; this is because the emergent SEDs calculated with the full models tend to agree well with the typical observed values (see Paper II). However factor $\lesssim 2$ differences do arise, largely because the empirical model does not allow spatial and/or time-dependent variations in the emergent SED (for example, very young stars in the galaxy nucleus tend to be much more obscured than older stars in the galaxy outskirts). We also compare a model with fixed UV/optical/IR fractions, but much higher UV/optical fractions than actually observed (red): (0.2, 0.3, 0.5) for the HiZ/Sbc/MW cases and (0.4, 0.4, 0.2) for the SMC. This artificially boosts the long-range radiation pressure, which leads to a nearly linear corresponding boost in the wind efficiencies.

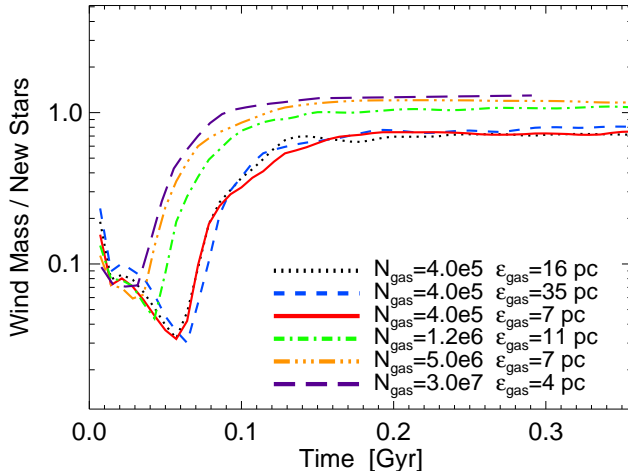


Figure A3. Resolution tests. We plot the wind mass-loading versus time (as Figure 6). We consider a “standard” (all feedback enabled) HiZ model at a series in mass and force resolution (N_{gas} is the number of gas particles in the star-forming disk, which determines the mass resolution; ϵ_{gas} is the force softening). The wind mass tends to increase at higher resolution as venting, mixing, and acceleration of filaments/clumpsstreams through a background medium can be more accurately resolved. But once we reach $\sim 10^6$ disk particles and ~ 10 pc resolution, the winds as well appear to converge (changing by $< 10\%$ going to higher resolution). Recall, the Jeans length in these galaxies is several hundred pc (Jeans mass $\gtrsim 10^8 M_{\odot}$), so *all* of these models formally resolve the Jeans scales. At lower resolution, our prescriptions do not have clear physical meaning.

the “boost” in the wind mass-loading is approximately linear in the UV/optical escape fraction, as predicted in § 4.3. This drives the inverse dependence of the wind mass loading on gas surface density (at otherwise fixed properties).

A1 Resolution Tests

In Figure A3 we consider a basic spatial and mass resolution study of the winds. We consider an otherwise identical “standard” HiZ run, with different particle number (mass resolution) and

force softening (spatial resolution).⁸ In Paper II the SFRs for this study are shown – they converge relatively quickly. In contrast, the winds show a clear, albeit not dramatic, resolution dependence. The fact that the higher-resolution runs converge to equilibrium more rapidly is not important – it is simply a consequence of the fact that most rapidly collapsing spatial scale resolved is on a smaller timescale as we go to higher resolution. But going from low to intermediate resolution, the equilibrium wind mass loading efficiency approximately doubles. At still lower resolution than we show here, the wind mass begins to drop exponentially. This is because the simulation can no longer resolve the phases of the ISM and “holes” for gas to accelerate out along. In addition, at low resolution the columns around each star particle (hence extinction of UV/optical light) will be over-estimated, since the clumpiness of the ISM is not correctly treated. Moreover at low mass resolution it requires very concentrated momentum to accelerate even single particles out of the disk – this is why the results appear to be more dependent on the mass resolution (N_{gas}), at least in the range we show here, than on the force resolution at fixed mass resolution. Finally, at low resolution in particular, it is well-known that SPH codes with energy and entropy conserving integration schemes produce artificial “surface tension” forces that suppress the acceleration gas streams through a porous or unstable medium. Once we reach intermediate resolution, however, the convergence even in the winds becomes quite good. From intermediate to standard resolution the wind mass loading changes by only $\sim 10 - 20\%$, and from standard to ultra-high resolution it changes by $< 5\%$.

⁸ For technical reasons to ensure quantities such as random number generation were identical in these runs, this set was run on the same set of processors and so does not overlap with our standard HiZ run shown earlier; but the results from that run are completely consistent with the standard-resolution case here.